

711-55-22

JPL Publication 90-56

Proceedings of the Second Airborne Synthetic Aperture Radar (AIRSAR) Workshop

June 7 and 8, 1990

Michael Kobrick
Editor

(NASA-CR-197342) PROCEEDINGS OF
THE SECOND AIRBORNE SYNTHETIC
APERTURE RADAR (AIRSAR) WORKSHOP
(JPL) 64 p

N95-70729
--THRU--
N95-70737
Unclass

Z9/43 0040781

November 15, 1990



National Aeronautics and
Space Administration

Jet Propulsion Laboratory
California Institute of Technology
Pasadena, California

ORIGINAL CONTAINS
COLOR ILLUSTRATIONS

Proceedings of the Second Airborne Synthetic Aperture Radar (AIRSAR) Workshop

June 7 and 8, 1990

Michael Kobrick
Editor

November 15, 1990



National Aeronautics and
Space Administration

Jet Propulsion Laboratory
California Institute of Technology
Pasadena, California

This publication was prepared by the Jet Propulsion Laboratory, California Institute of Technology, under a contract with the National Aeronautics and Space Administration.

ABSTRACT

The airborne Synthetic Aperture Radar (SAR) program at the Jet Propulsion Laboratory (JPL) commenced in 1970, when a coherent L-band radar, originally flown on an Aerobee rocket, was refurbished for flights on the Ames Research Center Convair 990 Airborne Laboratory. This airborne radar was flown throughout the 1970's, and was a pathfinder for the Apollo Lunar Sounder, Seasat, Magellan, and Shuttle Imaging Radars.

The current version is called AIRSAR, a three-frequency, fully polarimetric imaging radar, and flies on the National Aeronautics and Space Administration's (NASA's) new McDonnell Douglas DC-8 platform. The instrument serves both as a research tool for the development of new radar remote sensing techniques, and as a facility instrument gathering SAR data in support of scientific research programs conducted by principal investigators selected by NASA.

This publication contains papers presented at the Airborne Geoscience Workshop, held at JPL in June 1990. The investigators who attended the workshop have used AIRSAR data for work in geology, oceanography, ecology, hydrology, and remote sensing science. The papers reflect the diversity of applications of polarimetric SAR data, and indicate the types of scientific results that are expected to accrue from the several orbital radar sensors that will be launched during the 1990's.

CONTENTS

Calibration Experiments With DC-8 SAR Data: Anthony Freeman	1
Ground Truth Measurements for the Analysis of Airborne SAR Data Recorded Over Oberpfaffenhofen, FRG, 1989: T. Bayer, F. Wieneke, and R. Winter	8
Dutch X-band SLAR Calibration: J. S. Groot	14
Synthetic Aperture Radar Observations of the Greenland Ice Sheet: K. Jezek, J. P. Crawford, R. Bindenschadler, M. R. Drinkwater, and R. Kwok	21
Comparison of Active and Passive Microwave Signatures of Arctic Sea Ice: M. R. Drinkwater, J. P. Crawford, D. J. Cavalieri, B. Holt, and F. D. Carsey	29
River and Lake Ice Conditions as Determined From AIRSAR Imagery: Rae A. Melloh and Lawrence W. Gatto	37
Preliminary Results from the Maestro 1 Campaign Over the Black Forest: P. N. Churchill, G. De Grandi, and A. J. Sieber	43
Application of the Semivariogram Textural Classifier (STC) to SIR-B Data of Borneo: F. P. Miranda, J. A. MacDonald, and J. R. Carr	53
 APPENDIX	
A. Workshop Agenda	A-1

CALIBRATION EXPERIMENTS WITH DC-8 SAR DATA

ANTHONY FREEMAN, Jet Propulsion Laboratory, California Institute of Technology,
Pasadena CA, U.S.A.

ABSTRACT

This paper is a summary of some research activities in calibrating DC-8 SAR data conducted in 1989/90 by the author and others. Firstly, by examining the process of "symmetrization" in the production of DC-8 Stokes' matrix data, it is shown that an exact solution to the problem of calibrating this data exists, given certain assumptions. Secondly a new, more general, system model for radar polarimeters is proposed, together with a simple approach for verifying the model's validity. The importance of the orientation angle about the radar line of sight for some types of calibration devices is discussed and some results of an experiment to cross-calibrate the C-Band VV data from the DC-8 and DLR E-SAR sensors are presented.

THE PROBLEM OF CALIBRATING STOKES' MATRIX DATA

The basic problem in pol-SAR calibration (ignoring system noise for the moment) is to find the 'true' scattering matrix, S , from the measurement, Z , i.e.,

$$Z = Ae^{j\theta} \begin{pmatrix} 1 & \delta_2 \\ \delta_1 & F_1 \end{pmatrix} \begin{pmatrix} S_{HH} & S_{VH} \\ S_{HV} & S_{VV} \end{pmatrix} \begin{pmatrix} 1 & \delta_3 \\ \delta_4 & F_2 \end{pmatrix} = R^t S T \quad (1)$$

The term $Ae^{j\theta}$ shall be dropped in what follows, since we are only concerned with relative calibration between channels. In Kronecker delta (D-matrix) format, (1) then becomes:

$$Z_D = \begin{pmatrix} 1 & \delta_2 & \delta_4 & \delta_4\delta_2 \\ \delta_1 & F_1 & \delta_4\delta_1 & \delta_4F_1 \\ \delta_3 & \delta_3\delta_2 & F_2 & F_2\delta_2 \\ \delta_3\delta_1 & \delta_3F_1 & F_2\delta_1 & F_1F_2 \end{pmatrix} \begin{pmatrix} S_{HH} \\ S_{HV} \\ S_{VH} \\ S_{VV} \end{pmatrix} = D \underline{S} \quad (2)$$

In a recent paper, van Zyl (1990), has solved the problem for the case where $Z_D(HV) = Z_D(VH)$, whence, since S is fairly arbitrary, except for $S_{HV} = S_{VH}$, he is forced to assume that:

$$\delta_1 = \delta_3, F_1 = F_2 \text{ and } \delta_2 = \delta_4 \quad (3)$$

i.e., the second and third rows of the matrix in (2) must be equal. However, if we look at the "symmetrization" process which is applied in the DC-8 processor to the scattering matrix measurement, Z , before going to the Stokes matrix format, we see that what can happen is as follows. First, the relative phase between the HV and VH measurements, ϕ , is calculated, as an average over the whole image. Then, a phase shift, $-\phi$, is applied to the VH measurement and the "symmetrized" matrix HV term is calculated as:

$$Z'_{HV} = 0.5 [Z_{HV} + Z_{VH} \exp \{-j\phi\}] \quad (4)$$

The phase value, ϕ , is then saved and supplied with the Stokes matrix image in the header, for later phase calibration.

Without any loss of information, but assuming that the system crosstalk is sufficiently small that we can neglect terms of order δ^2 , and that $S_{HV} = S_{VH}$, what we have after "symmetrization" can be written as a 3 x 3 matrix premultiplying a 3-element vector, i.e.,

$$Z'_D = \begin{pmatrix} 1 & (\delta_2 + \delta_4) & 0 \\ (\delta_1 + \delta_3 e^{-j\phi})/2 & (F_1 + F_2 e^{-j\phi})/2 & (F_1 \delta_4 + \delta_2 F_2 e^{-j\phi})/2 \\ 0 & (F_1 \delta_3 + F_2 \delta_1) & F_1 F_2 \end{pmatrix} \begin{pmatrix} S_{HH} \\ S_{HV} \\ S_{VV} \end{pmatrix} = D' \underline{S'} \quad (5)$$

An exact solution to the problem of pol-SAR data calibration then exists and involves just finding $(D')^{-1}$. In a recent paper (Freeman 1990), it was shown that this exact solution can be found and that, for most DC-8 data examined so far, the solution offered by van Zyl (1990) is very close to it.

A NEW SYSTEM MODEL FOR RADAR POLARIMETERS

Errors in the gain differential between H and V receivers or transmitters may be present in many practical realizations of radar polarimeters (including the DC-8) and can be represented by a new system model:

$$\underline{Z} = A e^{j\phi} \begin{pmatrix} 1 & \delta_2 & \delta_4 & \delta_2 \delta_4 \\ \delta_1 & f_1 & \delta_4 \delta_1 & \delta_4 f_1 \\ \alpha_1 \delta_3 & \alpha_1 \delta_2 \delta_3 & \alpha_1 f_2 & \alpha_1 \delta_2 f_2 \\ \alpha_2 \delta_1 \delta_3 & \alpha_2 \delta_3 f_1 & \alpha_2 \delta_1 f_2 & \alpha_2 f_1 f_2 \end{pmatrix} \begin{pmatrix} S_{HH} \\ S_{HV} \\ S_{VH} \\ S_{VV} \end{pmatrix} \quad (6)$$

where α_1 and α_2 are complex constants, representing the (additional) gain or phase imbalance of the VH and VV measurements, with respect to the HH. In this representation, the overall gain or phase of each channel is independent of all the others.

Now let,

$$f'_2 = \alpha_1 f_2, \gamma = \frac{\alpha_2}{\alpha_1} \text{ and } \delta'_3 = \alpha_1 \delta_3 \quad (7)$$

so that (7) becomes:

$$\underline{Z}' = Ae^{j\phi} \begin{pmatrix} 1 & \delta_2 & \delta_4 & \delta_2 \delta_4 \\ \delta_1 & f_1 & \delta_4 \delta_1 & \delta_4 f_1 \\ \delta'_3 & \delta_2 \delta'_3 & f'_2 & \delta_2 f'_2 \\ \gamma \delta_1 \delta'_3 & \gamma \delta'_3 f_1 & \gamma \delta_1 f'_2 & \gamma f_1 f'_2 \end{pmatrix} \begin{pmatrix} S_{HH} \\ S_{HV} \\ S_{VH} \\ S_{VV} \end{pmatrix} \quad (8)$$

The parameter γ is a measure of the product of the gain error terms in the cross-pol. channel vs. the like-pol., i.e., $\left(\frac{HV}{HH} \frac{VH}{VV} \right)$. For example, if the receiver gains for cross-pol. returns are set 6 dB higher than for the like-pol. (as in the nominal NASA/ JPL DC-8 SAR set-up), and this gain differential is not removed, then γ would be 12 dB. γ can be considered as a measure of the departure of the system from the 2×2 model. γ can be complex, so that phase changes between channels are included. γ should be close to unity for a well-behaved system. If we can find γ , then we can easily force a transformation of the measurements, \underline{Z}' , into measurements made by a polarimeter for which the 2×2 model is valid, by dividing all the VV measurements by γ . Having made this transformation, external polarimetric calibration approaches, which usually assume a 2×2 model for the R and T matrices, can then be successfully applied to the data.

Measurement of γ

To measure γ externally, it is essential to use a target with known (and non-trivial) like-to cross-pol. backscatter ratio, e.g. HV/HH. A dihedral corner reflector rotated through 22.5° about the line of sight to the radar is one example of such a target. We prefer to use a Polarimetric Active Radar Calibrator (PARC) (Freeman et al. 1990), because of its wide beamwidth, selectable scattering matrix and relative insensitivity to azimuth and elevation pointing errors.

Consider the three PARC scattering matrices, written in vector form as:

$$S_x = \begin{pmatrix} 0 \\ 1 \\ 0 \\ 0 \end{pmatrix}, \quad S_y = \begin{pmatrix} 0 \\ 0 \\ 1 \\ 0 \end{pmatrix}, \quad S_z = \begin{pmatrix} \sin \alpha \cos \alpha \\ \cos^2 \alpha \\ -\sin^2 \alpha \\ -\sin \alpha \cos \alpha \end{pmatrix} \quad (9)$$

For S_z , α , which is the orientation angle of the PARC with respect to the local horizontal, is usually chosen to be 45° , 135° , 225° , or 315° . We shall examine the effects of small deviations of α from these nominal values later. It is straightforward to show that γ can be estimated from any of the above PARC signatures via:

$$\gamma = \frac{X_{11}X_{22}}{X_{21}X_{12}} \quad \text{or} \quad \frac{Y_{11}Y_{22}}{Y_{12}Y_{21}} \quad \text{or} \quad \frac{Z_{11}Z_{22}}{Z_{12}Z_{21}} \quad (10)$$

where the X, Y, and Z are the scattering matrices as measured by the radar. The measurement from the S_z PARC is the least sensitive to errors introduced by the background. Table 1 contains example estimates of γ from DC-8 data obtained over the Goldstone calibration site, and shows that without any correction applied to the receiver channels, γ can be quite significant. The corrections applied by the DC-8 processor to the data in 1989 improved on those applied in 1988. Note that in each case the phase of γ is small, which supports the conclusion that the error is just a gain problem. Table 2 shows an example of how the correction for γ can improve the calibration of the data, based on trihedral corner reflector signatures. Most of the DC-8 data issued to users from 1988 and 1989 campaigns should have γ sufficiently close to unity that the standard 2×2 R and T matrix model is applicable. The PARC's at the Goldstone site allow periodic system checks on whether the appropriate correction factors are being used in the processor.

THE IMPORTANCE OF THE ORIENTATION ANGLE, α

Four different types of targets were deployed by the DLR team at a site in Oberpfaffenhofen, FRG, with scattering matrices :

$$\text{Trihedral} \begin{bmatrix} 1 & 0 \\ 0 & 1 \end{bmatrix} \quad 45^\circ \text{ PARC} \begin{bmatrix} \cos(\alpha + 45) \sin(\alpha + 45) & \cos^2(\alpha + 45) \\ -\sin^2(\alpha + 45) & -\sin(\alpha + 45) \cos(\alpha + 45) \end{bmatrix}$$

Table 1: γ -values Estimated From PARC's at Goldstone Calibration Site

#	Type	L-Band		C-Band		P-Band	
		Ampl.	Phase	Ampl.	Phase	Ampl.	Phase
1	20 MHz (No. Cal.) ¹	-8.04 dB	3.5°	-8.8 dB	-1.1°	-12.2 dB	-4.1°
2	20 MHz (With Cal.) ²	0.21 dB	1.7°	-0.6 dB	-2.9°	0.16 dB	-1.7°
3	40 MHz (With Cal.) ²	0.5 dB	5.2°	0.03 dB	7.4°	1.02 dB	-12.5°
4	20 MHz (With Cal.) ³	1.8 dB	2.3°	—	—	—	—
5	20 MHz (With Cal.) ³	—	—	0.98 dB	4.2°	—	—

1 No correction algorithm

2 With 1989 correction algorithm

3 With 1988 correction algorithm

Table 2: L-Band Trihedral Corner Reflector Signatures

	After Calibration		
	Before Calibration	No γ -correction	With γ -correction
HH/VV ampl.	-0.5 dB	-0.6 dB	-0.6 dB
HH/VV phase	75°	-3°	-1°
HV/HH ampl.	-17 dB	-19 dB	-30 dB
VH/HH ampl.	-16 dB	-22 dB	-29 dB

$$0^\circ \text{ dihedral} \begin{bmatrix} \cos 2\alpha & \sin 2\alpha \\ \sin 2\alpha & -\cos 2\alpha \end{bmatrix} 45^\circ \text{ dihedral} \begin{bmatrix} \cos 2(\alpha + 45) & \sin 2(\alpha + 45) \\ \sin 2(\alpha + 45) & -\cos 2(\alpha + 45) \end{bmatrix} \quad (11)$$

where α is an orientation angle about the line of sight between the target and the radar. Note that only the trihedral is insensitive to rotation errors. After calibration of the data, any residual channel imbalances for the other targets could be due to rotation errors between the target frame-of-reference and the radar frame-of-reference. Assuming this to be the case, we obtain the rotation error estimates given in Table 3.

Table 3: H-V Polarization Coordinate Angles, α , Estimated From Calibration Device Signatures

Parameter	form	α -estimate
PARC HV/HH	$\cot(\alpha + 4)$	$+0.7^\circ$
PARC VH/HH	$-\tan(\alpha + 45)$	$+0.9^\circ$
45° dihedral (0.7 m):		
HV/HH	$\tan 2(\alpha + 45)$	$\pm 3.7^\circ$
VH/HH	$\tan 2(\alpha + 45)$	$\pm 3.6^\circ$
45° dihedral (1 m):		
HV/HH	$\tan 2(\alpha + 45)$	$\pm 0.3^\circ$
VH/HH	$\tan 2(\alpha + 45)$	$\pm 0.3^\circ$
0° dihedral:		
HV/HH	$\tan 2\alpha$	$\pm 2.3^\circ$
VH/HH	$\tan 2\alpha$	$\pm 3.5^\circ$

Of course, there are several sources of errors which could give rise to these results, including background clutter contributions, device orientation errors, polarization impurity, as well as the roll, yaw, and pitch of the aircraft. The question is, what degree of sensitivity is required by the scientist using polarimetric radar data?

CROSS-CALIBRATION BETWEEN DC-8 SAR AND E-SAR DATA

Based on trihedral corner reflector signatures, images of the DLR calibration site obtained by the DC-8 SAR and the C-Band E-SAR system were separately calibrated, then compared. The results are highlighted in Table 4. Note the relatively small fluctuations in the trihedral cross sections at VV. Five different areas within the scene were selected for comparison of their σ° and contrast (standard deviation over mean ratio). The values are within 2 dB of each other, except for the urban area, where we might expect the backscatter to be highly variable, in any case.

For the DC-8 data, which is one-look, we would expect the contrast for a uniform target to be ~ 1.0 . Only the urban area shows significant departure from uniformity in Table 4. In the E-SAR data, which is four-look, we would expect the contrast to be ~ 0.5 for a uniform target. In this case, both the urban area and the forest show significant departures from uniformity. We might anticipate this result due to the better resolution of the E-SAR system, which is ~ 2.4 m x 4.0 m (vs. 4.5 m x 11.0 m for the DC-8). Thus, for forested areas, the E-SAR system would have fewer scatterers per resolution cell, which tends to increase image contrast (or texture).

Table 4: Comparison of Results From the DC-8 and E-SAR Data After Calibration

Targets (RCS)	DC-8 SAR				E-SAR	
	HH		VV		VV	
Trihedrals	29.1 (± 0.7) dB		29.1 (± 0.3) dB		29.3 (± 0.3) dB	
45° PARC	50.7 dB		50.9 dB		50.0 dB	
Areas (σ°)	dB	σ/μ	dB	σ/μ	dB	σ/μ
Runway	-19.3	1.15	-17.7	0.95	-18.9	0.53
Grass	-13.1	0.93	-13.8	0.98	-14.1	0.55
Urban	2.9	2.86	-1.2	2.22	-6.4	3.03
Field	-9.7	1.02	-9.9	1.01	-8.1	0.52
Forest	-7.5	1.03	-7.4	1.00	-8.1	0.66

ACKNOWLEDGMENTS

Part of the work described in this paper was carried out by the Jet Propulsion Laboratory, California Institute of Technology, under a contract with the National Aeronautics and Space Administration. The author would like to thank J. Klein, P. Olivier, P. Dubois, the DLR team, and the DC-8 SAR team for their contributions to this work.

REFERENCES

- van Zyl, J.J. 1990. A technique to calibrate polarimetric radar images using only image parameters and trihedral corner reflectors. *IEEE Trans. Geoscience and Remote Sensing*. Vol. 28, No. 3, May 1990, pp. 337–348.
- Freeman, A. 1990. An “exact” solution to the problem of calibrating Stokes’ matrix format polarimetric radar data. *Proc. IGARSS '90*. Univ. of Maryland, MD, U.S.A., 1990.
- Freeman, A., Shen, Y., and Werner, C. 1990. Polarimetric SAR calibration experiment using active radar calibrators. *IEEE Trans. Geoscience and Remote Sensing*. Vol. 28, No. 2, March 1990, pp. 224–240.

GROUND TRUTH MEASUREMENTS FOR THE ANALYSIS OF AIRBORNE SAR DATA RECORDED OVER OBERPFAFFENHOFEN, FRG, 1989

T. Bayer*, F. Wieneke**, R. Winter*

* German Aerospace Research Establishment DLR
Oberpfaffenhofen

** Institute for Geography
University of Munich

Introduction

As a preliminary investigation to the joint multiparameter SIR-C/X-SAR shuttle experiment of NASA/JPL (USA), DLR (FRG), and PSN (Italy) which is scheduled for the year 1992 [7] an airborne SAR campaign was conducted over Oberpfaffenhofen, FRG, in August 1989. Primarily this campaign was planned to test and verify equipment and algorithms developed at the DLR to calibrate multifrequency polarimetric SAR data.

Oberpfaffenhofen is designated as one of the super test sites for the SIR-C/X-SAR experiment which will be imaged under all circumstances except severe mission errors. A super test site drives radar parameters and look directions and the recorded SAR data will be calibrated. In addition ancillary data will be available for the site [9].

During the airborne SAR campaign conducted in the week of August 14th 1989 various sensor types were used to record remote sensing data over the calibration test site and its vicinity.

- the polarimetric DC-8 JPL-SAR (P-, L-, C-band),
- the DLR airborne SAR (C-, X-band),
- color infrared aerial photography (DLR) and
- the truck-mounted scatterometer (C- and X-band) of the Institute for Navigation, University of Stuttgart (INS).

Because of this variety of different sensor types used and out of the fact that sufficiently large forested and agriculturally used areas were planned to be covered by these sensors, the interest of several German research groups involved in investigations concerning SAR land applications arose. The following groups carried out different ground-truth measurements:

- University of Bonn, Institute for plant cultivation (plant morphology and moisture content),
- University of Braunschweig, Institute for Geography (soil moisture and surface roughness),
- University of Freiburg, Institute for Geography (dielectric soil properties, landuse),
- University of Munich, Institute for Geography (landuse inventory, plant, surface, and soil parameters).

This paper presents the joint ground truth activities of the Institute for Geography, University of Munich, and the German Remote Sensing Data Centre of the DLR.

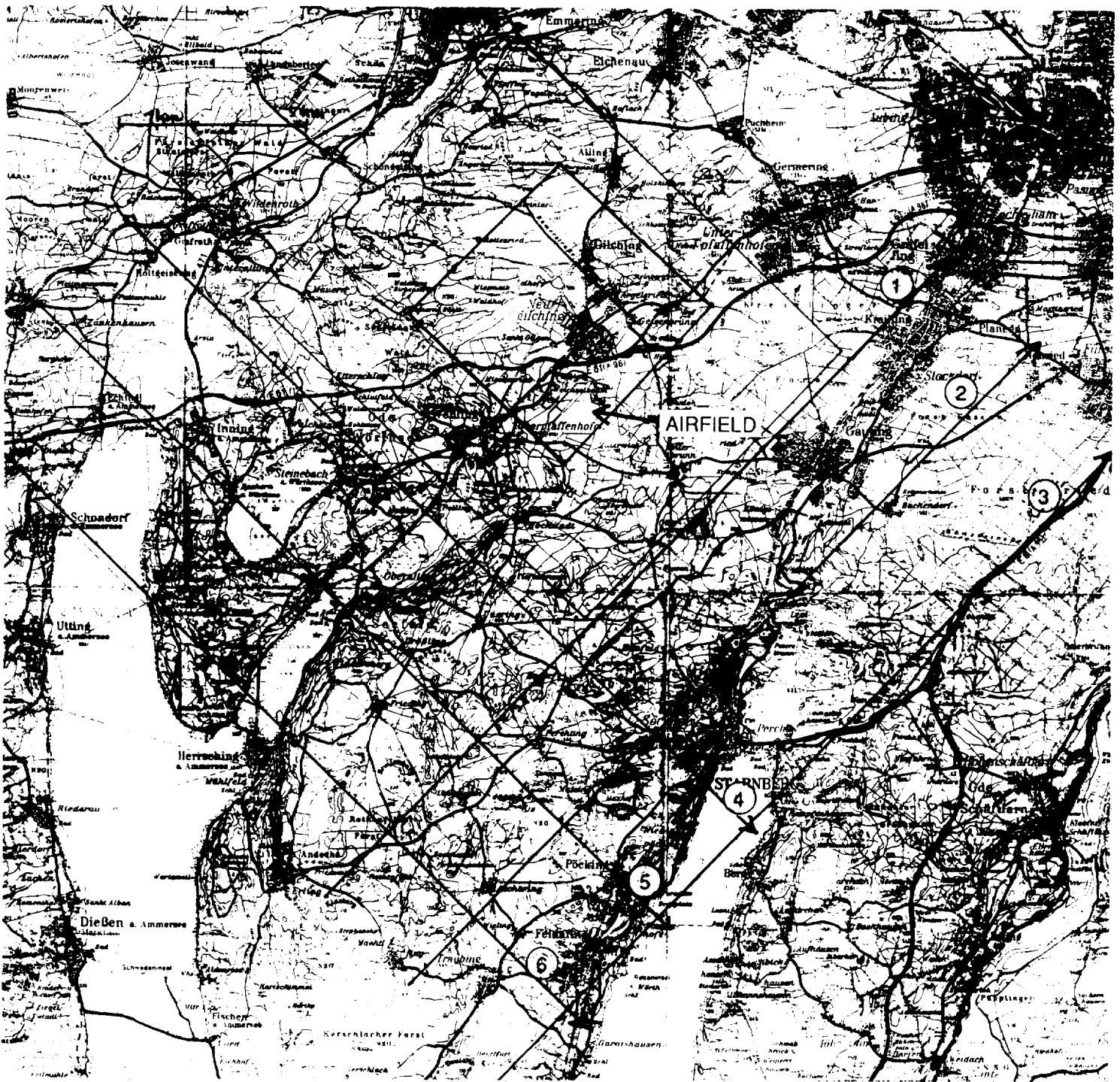


Fig.1: Map of Oberpfaffenhofen and vicinity containing the DC-8 flight paths and the centre frame imaged by all paths.

ORIGINAL PAGE IS
OF POOR QUALITY

The Test Site

Oberpfaffenhofen is the location of the DLR facilities and of a connected airfield and is situated about 30 km south-westward of the city of Munich in southern Bavaria (s. Fig. 1).

The natural landscape character and the relief forms of the area around Oberpfaffenhofen are of pleistocene origin. Hilly moraines of the last two ice ages alternate with fluvial gravel plains. The relative differences of height in this area of low relief energy do not exceed 60 m to 80 m. The dominant soil types in the region are Rendzinas and thin Luvisols covering the younger gravel moraines and the gravel plains and thicker Luvisols developed on loess accumulations covering the elder moraines.

About 50 % of the whole test site area which covers approximately 100 km² is covered by forest, mainly coniferous and mixed deciduous/coniferous forest. About 40 % of the area is agriculturally used with the dominant crop types being meadows, cereal, corn and some root crops. The sizes of the parcels of land being cultivated are typically relatively small ranging from below 5000 m² (which is 0.5 ha) to mostly no more than about 2 to 3 ha. The remaining 10 % of the area is covered by village and suburban areas.

The SAR Data

Two different airborne SAR sensors have been involved in the campaign over Oberpfaffenhofen, the polarimetric JPL SAR and the DLR SAR.

The multifrequency SAR of the Jet Propulsion Laboratory (JPL), Pasadena, is mounted aboard a DC-8 airplane and records polarimetric SAR data in the P-, L- and C-band simultaneously. Its resolution is given in [11] with 3 m in azimuth and 7.5 m in range direction. The width of the recorded swath is approximately 12 km; the pixel spacing in the resulting images processed with 4 looks is 12 m by 12 m. The total size in pixels for one recorded scene is 1024 by 1024 pixels. A description of the JPL airborne SAR system is given in [11].

Six data takes were flown over Oberpfaffenhofen on August 18th, 1989, at a height of about 7000 m above ground. Three of the data takes were flown in a SW-NE direction parallel to the runway of the Oberpfaffenhofen airfield which was the centre of the calibration activities; three data takes were flown perpendicular to the runway in a NW-SE direction (s. Fig. 1). The data recorded on these six flight passes will not only provide polarimetric SAR data in three frequencies but will also provide an opportunity to study incidence angle effects at two different SAR viewing angles onto specific ground target features. The incidence angles of the radar beams on the centre of the airfield nominally have been 30°, 45°, and 55° for the three flight passes in each direction.

The DLR SAR (E-SAR) is mounted aboard a Do-228 airplane and is able to record VV-polarized SAR data in either one of three bands (L-, C- or X-band). During the campaign it was operated in C- and X-band modes and recorded data with an azimuth resolution of 1.7 m and a range resolution of 2 m over a swath width of about 4 km. The resulting image pixel spacing in the processed SAR images is 1.4 m. A description of the E-SAR system is given in [5].

The E-SAR system has been flown on the same six tracks as the DC-8 system at a height of about 3000 m above ground. Two additional tracks have been flown to especially cover agriculturally used areas for the purpose of landuse investigations.

Calibration of the recorded SAR data is done at the JPL as well as at the DLR [3, 4].

Ground Truth Measurements

The Institute for Geography of the University of Munich together with the German Remote Sensing Data Centre of the DLR carried out a ground truth campaign in the area of Oberpfaffenhofen in the week of August 14th 1989. The measurements performed during this campaign concentrated on the following points:

- land use inventory based on agricultural maps 1:5000,
- measurement of plant and cultivation parameters,
- measurement of bare soil surface roughness,
- measurement of soil moisture.

Landuse Inventory

From August 14th to August 20th 1989 a detailed land use inventory was conducted in the test site area northward of Oberpfaffenhofen. The inventory was based on agricultural maps in the scale 1:5000 and covered an area of approximately 12 km by 12 km. The field boundaries were measured and registered onto the maps. The crop type and/or the cultivation stage was recorded on standardized form sheets for a total of about 600 fields.

Plant and Cultivation Parameters

For about 50 % of the registered fields a variety of plant and cultivation parameters was recorded and measured.

For crop fields the following parameters were recorded:

- type of crop and phenology,
- cultivation direction,
- plant height,
- row density,
- plant density per meter of a row,
- slope and aspect (if any),
- special observations of plant conditions through ground photography documentation.

For harvested and bare soil fields the following parameters were recorded:

- type of cultivation,
- direction of cultivation,
- for stubble fields:
 - stubble type and height,
- slope and aspect (if any),
- special observations of plant conditions through ground photography documentation.

Roughness of bare soil fields

For each cultivation type of bare soil fields the surface roughness was measured for a significant number of test fields. The measurement of a profile of the surface roughness for a specific test field was carried out using a gridded panel (130 cm by 45 cm) with a 2-cm grid which was put into the test field and photographed. The panel was put in and photographed four times per field; twice parallel and twice perpendicular to the cultivation direction of the field. Through measurement of the relative differences in height along these profiles the surface roughness may be estimated as the standard deviation of height in each direction [2].

Soil moisture measurement

The gravimetric soil moisture of the top 3 cm to 5-cm soil layer was measured for ten selected test fields with different soil types and moisture conditions at the day and time of the DC-8 flight over the test site. From each field a total of ten samples was taken, two at each of five different locations.

One horizontal profile of the soil moisture was measured over a distance of 250 m with samples taken every 10 m. Two parallel samples were taken at each point.

The wet samples were weighed right after sampling using a digital weighing machine. Afterwards they were dried at 120°C and weighed again to determine the gravimetric moisture content of the soil samples.

On the day of the DC-8 flight there had been strong rain in the forenoon after a period of many hot and dry days. Until the time of the flight (afternoon between 16:30 and 18:00) the top layer of the soil had been dried already dependent on relief and soil type conditions. Thus significant changes in the gravimetric soil moisture occurred along the measured profile ranging from 15g/100g to 40g/100g which we hope to verify within the SAR data.

Processing Steps of the Recorded Data

The gathered ground truth data and the recorded SAR data are processed digitally and will be stored in a common data base which is part of a geographical information system (GIS).

The maps (1:5000) containing the field boundaries have been digitized and stored within the GIS. For each field represented by an outlining polygon the recorded ground truth measurements are stored as additional features in the form of tables within the database. These values will provide sources for parameter input into modelling techniques for the analysis and interpretation of the information content of the polarimetric SAR data.

The recorded SAR images will have to be geocoded and coregistered with the agricultural maps, which are present in the German Gauß-Krüger map coordinate system (a transversal Mercator projection). This will be done by means of control points that are identified in the maps as well as in the images and by the application of a polynomial adjustment. This method is considered to be of sufficient accuracy in the case of airborne SAR data recorded over flat terrain [6].

Radiometric effects of incidence angle variations caused by the swath width and by terrain undulations will be investigated and existing methods for their reduction will be applied [1].

For selected test fields of different surface cover characteristics the frequency and polarimetric signatures [10] will be calculated in order to provide means for classification attempts of the SAR images. The applicability and the use of a newly developed signature analysis tool of polarimetric SAR data based on the Fourier analysis of the polarization signatures [8] will be investigated.

Making use of the geocoded images and the recorded parameters for the agricultural fields, the derivation of empirical backscatter models describing the statistical behaviour of the SAR data will be attempted.

Yet these intentions are strongly dependent on calibrated SAR data. The process of calibration of the DC-8 polarimetric SAR data at the DLR is still on the way and an absolute calibration is feasible for C-band and L-band data whereas for the P-band data this seems to be impossible because in the scene that is available at this time (heading 42°, incidence angle on the runway 45°) none of the corner reflectors on the airfield of Oberpfaffenhofen can be identified. The gathered ground truth data may provide a possibility to carry out at least a relative calibration of this data.

Acknowledgements

The authors thank all the participants of the Institute for Geography, University of Munich, at the ground truth campaign for their motivation and their voluntary engagement, without which these extensive measurements could not have been carried out.



Fig.2: Participants of the ground truth campaign of the University of Munich, Institute for Geography

References

- [1] BAYER, T., WINTER, R., SCHREIER, G. (1990): Terrain Influences in SAR Backscatter and Attempts to their Correction. Submitted to be published in IEEE Transactions on Geoscience and Remote Sensing.
- [2] CIHLAR, J., DOBSON, M.C., SCHMUGGE, T. ET AL. (1987): Procedures for the Description of Agricultural Crops and Soils in Optical and Microwave Remote Sensing Studies. In: Int. Jour. of Remote Sensing, Vol.8, Nr.3, p.427-439.
- [3] FREEMAN, A. (1990): An "Exact" Solution to the Problem of Calibrating Stokes Matrix Polarimetric SAR Data. In: Proc. IGARSS'90, Washington.
- [4] FREEMAN, A., CURLANDER, J.C., HEEL, F. ET AL. (1990): Preliminary Results of the Multi-Sensor, Multi-Polarization SAR Calibration Experiments in Europe 1989. In: Proc. IGARSS'90, Washington.
- [5] HORN, R. (1989): C-Band SAR Results obtained by an Experimental Airborne SAR Sensor. In: Proc. IGARSS'89, Vancouver, p.2213-2216.
- [6] IPCG (Ed.)(1987): Synthetic Aperture Radar Image Rectification Techniques. Proc. 1st Int. Workshop on Image Rectification Techniques for Spaceborne Synthetic Aperture Radar, Loipersdorf, DIBAG Report 29, Graz.
- [7] NASA (Ed.): The Early Earth Observing System Reference Handbook.
- [8] RECK, M., SCHREIER, G. (1990): Fourier Series Presentation of SAR Polarimetric Scattering Signatures. In: Proc. IGARSS'90, Washington.
- [9] RUZEK, M. (1990): SIR-C/X-SAR Strawman Mission Scenario. SIR-C/X-SAR Team Meeting, January 1990, Pasadena.
- [10] van ZYL, J.J., ZEBKER, H.A., ELACHI, C. (1987): Imaging Radar Polarization Signatures: Theory and Observation. In: Radio Science, Vol.22, Nr.4, p.529-543.
- [11] van ZYL, J.J. (1989): Imaging Radar Polarimetry. In: Report of NFS Workshop on Future Directions in Electromagnetics Research, July 1989, Boston, p.296-300.

P-1

Dutch X-band SLAR Calibration

J.S. Groot
FEL-TNO
PO box 96864
The Hague - The Netherlands

May 29, 1990

1 Introduction

In August 1989 the NASA/JPL airborne P/L/C-band DC-8 SAR [1] participated in several remote sensing campaigns in Europe. Amongst other test sites, data were obtained of the Flevopolder test site in the Netherlands on August the 16th. The Dutch X-band SLAR was flown on the same date and imaged parts of the same area as the SAR. To calibrate the two imaging radars a set of 33 calibration devices was deployed. 16 trihedrals were used to calibrate a part of the SLAR data.

This short paper outlines the X-band SLAR characteristics, the experimental set-up and the calibration method used to calibrate the SLAR data. Finally some preliminary results are given.

2 The Dutch X-band SLAR

In 1979 the development of a digital X-band sideways looking airborne radar (SLAR) was initiated in the Netherlands. After its completion the system was modified/upgraded several times. One of the major improvements was the addition of an internal calibration. Table 1 presents some relevant characteristics of the system in its present form.

The final product obtained by processing the raw SLAR data is a radiometrical and geometrical correct image [2]. The radiometric corrections are achieved by using, amongst others, the measured antenna pattern, INS (Inertial Navigation System) and the already mentioned internal calibration. The internal calibration circuit uses a delay line that delays part of the transmitted pulse power. The delayed signal is fed into the receiver. It produces a response at the output of the radar which is a measure for the transmitted power. This can be used to compensate for the changes occurring in the radar system (output power of the magnetron etc.). Data obtained during different flights can thus be intercalibrated.

The pixel size of the final product is 7.5 m * 7.5 m on the ground. The scattering coefficient γ is related to the pixel value pv by

$$\gamma = \frac{pv}{5} + C \text{ [dB]} \quad (1)$$

The constant C can be determined from external calibration using targets of which the radar cross section is known with sufficient accuracy.

3 The experiment

On August 16, 1989 three different airborne remote sensing instruments imaged parts of the Flevopolder and the Veluwe. The Flevopolder is a reclaimed land area situated in the center of the Netherlands. It is mainly used for agriculture. The Veluwe is a forested area. The three instruments were the NASA/JPL P/L/C polarimetric SAR, the Dutch X-band SLAR, and the

CAESAR, a Dutch multispectral optical scanner. All three instruments obtained images of the test area in the Flevopolder with their flight tracks oriented at 56° with respect to the geographical North. The SAR and SLAR also imaged the same Flevopolder test area under a different track angle of about 116° . The latter tracks extended into the Veluwe.

To calibrate the SAR and SLAR imagery of the Flevopolder and the Veluwe 20 trihedrals, 6 dihedrals and 7 PARCs were placed in four bare soil fields ($\gamma \approx 0 \rightarrow -5$ dB at X-band, incidence angle $\approx 45^\circ$) in the Flevopolder. The PARCs, owned and deployed by the Jet Propulsion Laboratory, cover L- and C-band. The PARCs and dihedrals are to be used for SAR calibration. The trihedrals can be used for the calibration of the SAR and SLAR. Calibration of the SLAR and SAR data is a joint effort of the FEL-TNO and JPL, carried out in preparation to SIR-C experiments.

Figure 1 gives the set-up for calibration field 2. Similar set-ups were used on calibration fields 1 and 3. The six dihedrals were all placed in calibration field 4. The SAR and SLAR flew almost parallel to the longer side of the rectangular field. The positions of the devices were surveyed with an accuracy better than 0.5 m. The trihedral corner reflectors used differ from the commonly used ones by having two triangular side plates and a square base plate [3]. The main advantage of these reflectors is the improved insensitivity to multipath reflections. Reflectors of three different sizes were used, the dimensions of a side of the square base plate being 1.43, 0.93 and 0.65 m. The arrows in figure 1 indicate the azimuthal pointing angle of the devices. The leftmost corner reflector is pointed in such a way that its response can be used to calibrate the Veluwe images. To avoid overlap of the reflector responses the devices were placed on an oblique line (with respect to the SAR and SLAR tracks). A total of 16 trihedrals could be used to calibrate the SLAR imagery of the Flevopolder.

Figure 2 presents a SLAR image containing calibration field 2 (in the center). Near range is at the bottom of the image. The responses of the five corner reflectors are clearly visible. Pixel size is 7.5 m * 7.5 m. Total dimensions of the image are 5.57 km * 5.24 km (horizontal * vertical). Flying height was 3.0 km, ground speed 110 m/s.

4 Calibration method

The precision of external calibration of a radar system with trihedral corner reflectors is determined by the calibration-target-to-background radar cross-section ratio [4]. To maximize this ratio it is necessary to deploy large corner reflectors against a low background. This ratio exceeds 20 dB for the largest reflectors used in this experiment. This leads to a calibration uncertainty of at most 1 dB.

The ‘integral method’ proposed in [5] incorporates subtraction of the mean background contribution. This diminishes the calibration uncertainty, provided the background is sufficiently homogeneous. Another advantage is that the result does not depend on the resolution. It can therefore also be used to calibrate partially focused SAR images.

The integral method was used to determine the (absolute) scattering coefficient of the four fields in which the 16 corner reflectors were placed. For this analysis the uncorrected raw SLAR data was used. An example of a raw SLAR image of an area containing calibration field 2 is given in figure 3. The horizontal white line at the bottom of the image is caused by cross-talk of the transmitted radar pulse. The smaller line just above it is caused by the internal calibration circuitry. Calibration field 2 and the corner reflectors are at the top of the image. The raw data are used to maximize the number of pixels contributing to the integral of the corner reflector response, thereby maximizing the accuracy of this calibration method.

The (uncalibrated) scattering coefficient of a field can also be determined from the processed SLAR image. Substitution of this value and the calibrated value obtained by the integral method in eq.(1) determines the calibration constant C . Because the processed SLAR images are already geometrically and radiometrically corrected this constant enables one to obtain the calibrated scattering coefficient for every part of the image.

5 Preliminary results

Table 2 gives the results. The leftmost four columns contain the calibration field number, the incidence angle (approximately constant per field), a unique corner reflector number and the radar cross section of the reflector, respectively. The γ column contains the scattering coefficients of the bare soil fields in which the reflectors were situated. They are computed from raw SLAR data with the integral method, as pointed out in the previous paragraph. The rightmost column gives the calibration factor C of eq.(1).

A first thing to note is that the γ values are higher than the expected $\gamma \approx 0 \rightarrow -5$ dB. Moreover, it appears that the scattering coefficient of a field generally decreases with decreasing corner reflector cross sections. A possible explanation is that the cross sections of the corner reflectors are smaller than theory predicts, with the deviation becoming larger for larger reflectors. This could be the case, because making reflectors with plates flat to within a few millimeters connected at right angles to each other becomes progressively difficult with increasing reflector size. Although this can present problems for this X-band radar data, it possibly does not influence calibration of the P/L/C band SAR data. At these wavelengths the constructional demands are less stringent.

Table 3 contains the calibration constants obtained when the results of the corner reflectors for each of the three different sizes are averaged. For example, the constant is -29.2 ± 0.6 for the reflectors 2,9,23 and 32 of approximately 45 dBm^2 (at X-band). If one assumes that the value of -33.4 dB computed from the results of the smallest reflectors is the right one, it must be concluded that the X-band cross section of the largest reflectors is about 4 dBm^2 lower than those predicted by theory.

Another possible explanation for the unexpected results is malfunctioning or saturation of the SLAR. However, the laboratory measurements conducted in the past do not provide any evidence for this. From theory it can be shown that even the largest corner reflectors are well below the saturation level of the receiver.

6 Summary and conclusions

In August 1989 an experiment took place with several remote sensing instruments in the Flevo-polder test area in the Netherlands. One objective was to calibrate the Dutch X-band SLAR data obtained. 16 trihedrals of 3 different sizes placed in 4 bare soil fields were used to accomplish this. The scattering coefficients computed from the raw data of the Dutch X-band SLAR using the 16 corner reflectors turned out to depend on the reflector cross section: smaller cross sections led to smaller scattering coefficients. A possible explanation is that the cross sections of the larger used corner reflectors are lower than theory predicts. To verify this, it is planned to measure the cross section of some of the used corner reflectors in the near future.

REFERENCES

1. D.N.Held et al., "The NASA/JPL Multifrequency, Multipolarization Airborne SAR System", Proc. IGARSS'88, Edinburgh, Scotland, 1988, pp.345-350.
2. P.Hoogeboom et al., "An Algorithm for Radiometric and Geometric Correction of Digital SLAR Data", IEEE Transactions on Geoscience and Remote Sensing, vol. GE-22 no. 6, November 1984.
3. K.M.Keen, "New Technique for the Evaluation of the Scattering Cross-Sections of Radar Corner Reflectors", IEE Proceedings, Vol.130, No.5, August 1983.
4. F.T.Ulaby et al., Microwave Remote Sensing, volume II, pp.768-770.
5. A.Haskell, presentation at Remote Sensing workshop, London, 1982.

frequency transceiver	transmitted power	9.4 GHz, HH-polarized
	pulse length	25 kW
	pulse repetition frequency	50 ns
digitalisation	sampling frequency	200 Hz
	bits per sample	50 MHz (20 ns)
final pixel size		8
resolution	across track	7.5 m * 7.5 m
	along track	7.5 m
	radiometric	10 mrad (two-way)
aircraft		0.3 dB
flying height		Metro II
ground speed		100-6000 m
		100 m/s

Table 1: SLAR characteristics

field	$\theta_{\text{incidence}}$	corner	σ	γ	C
	$^{\circ}$		dBm^2	dB	dB
1	37.4	2	45.5	2.8	-29.5
"	"	3	38.1	-1.2	-33.5
"	"	4	38.1	0.1	-32.2
"	"	5	31.8	-1.7	-34.0
"	"	6	31.8	-1.4	-33.7
2	48.8	9	45.4	2.0	-29.9
"	"	10	38.0	-0.5	-32.4
"	"	11	38.0	-0.4	-32.3
"	"	12	31.7	-2.7	-34.6
"	"	13	31.7	0.0	-31.9
3	48.0	23	45.3	2.2	-28.5
"	"	22	37.9	-0.2	-32.2
"	"	21	37.9	-0.9	-31.6
"	"	20	31.6	-2.3	-33.0
"	"	19	31.6	-2.6	-33.3
4	43.1	32	45.2	2.7	-29.0

Table 2: Preliminary calibration results

corners	σ_{app}	\bar{C}
	dBm^2	dB
2,9,23,32	45	-29.2 ± 0.6
3,4,10,11,21,22	38	-32.4 ± 0.6
5,6,12,13,19,20	32	-33.4 ± 0.9

Table 3: Calibration constant C

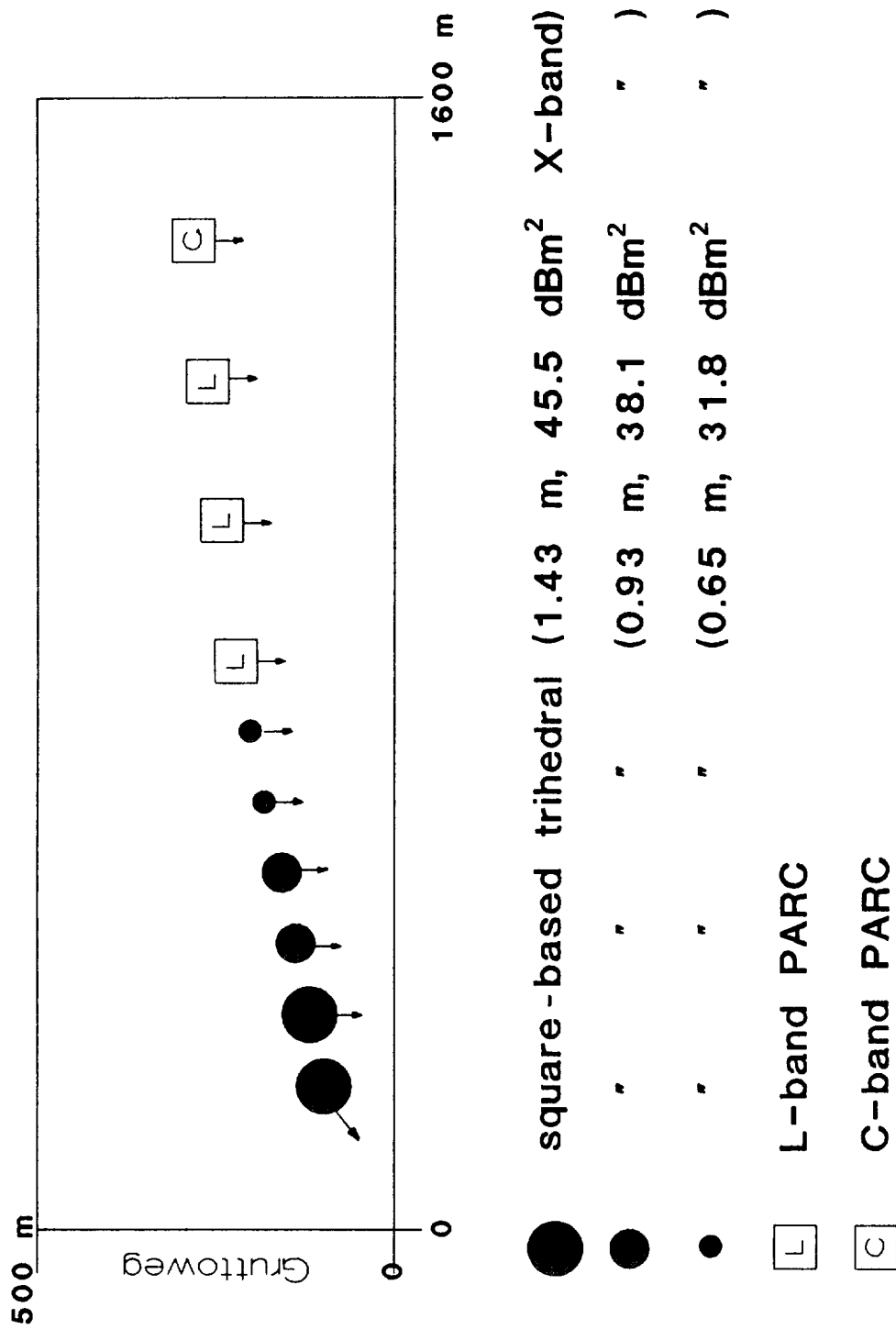


Figure 1: Placement of the calibration devices in calibration field 2

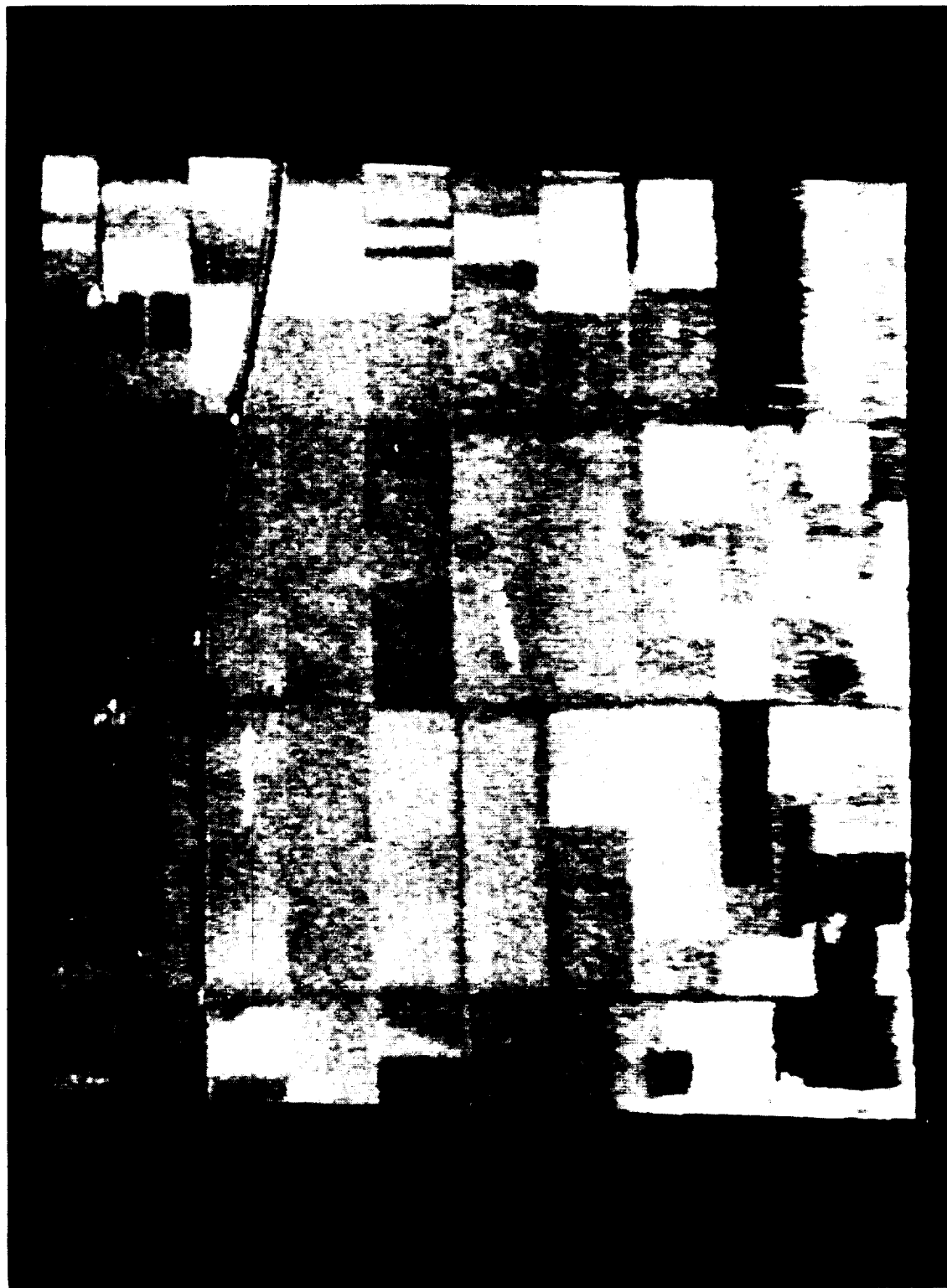


Figure 2: Processed SLAR image including calibration field 2

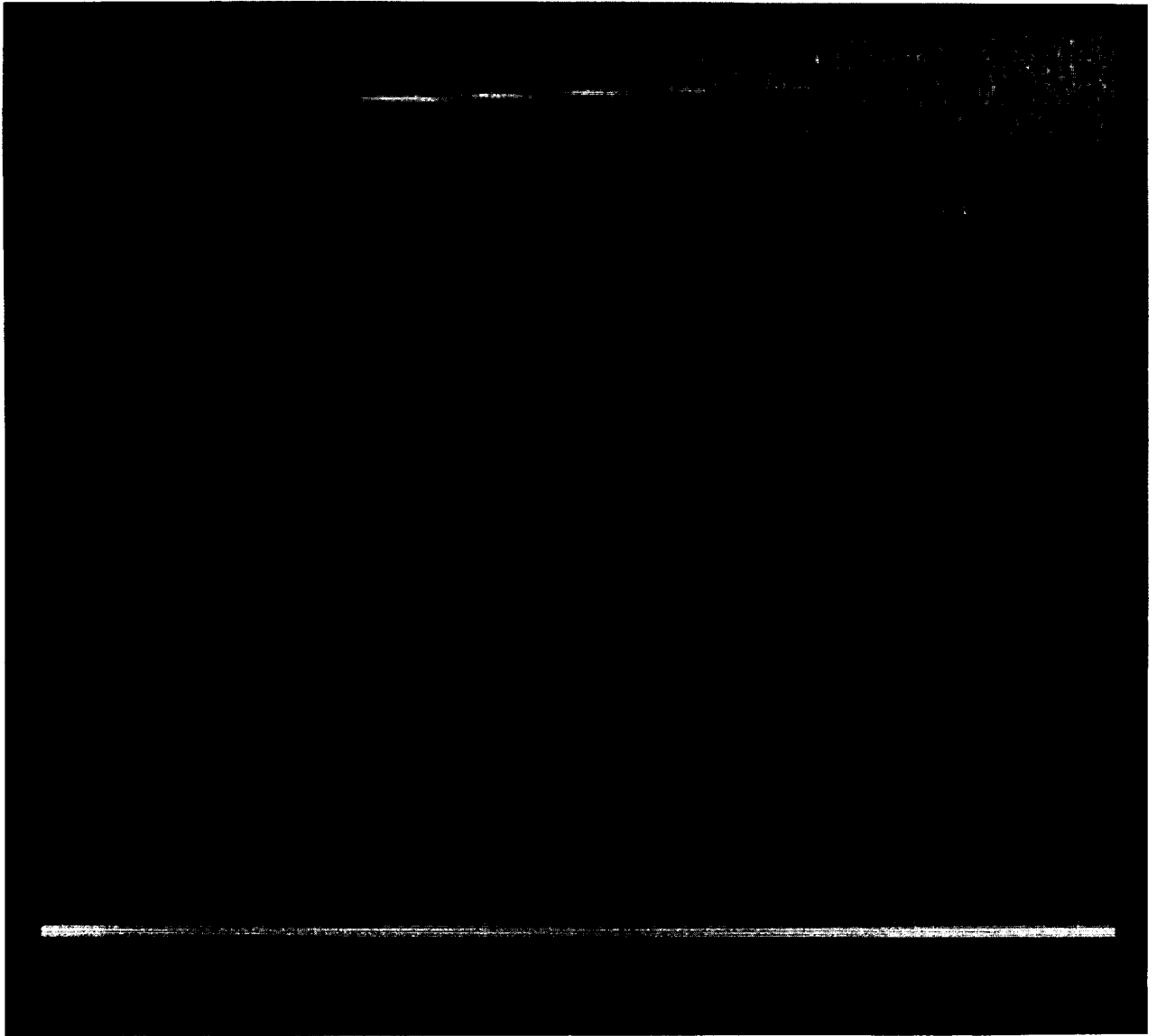


Figure 3: Raw uncorrected SLAR image including calibration field 2

Synthetic Aperture Radar Observations of the Greenland Ice Sheet

JEZEK, K. (Byrd Polar Research Center, The Ohio State University, Columbus, Ohio, USA)

CRAWFORD, J. P. (Jet Propulsion Laboratory, California Institute of Technology, Pasadena, California, USA)

BINDSCHADLER, R. (NASA Goddard Space Flight Center, Greenbelt, Maryland, USA)

DRINKWATER, M. R., and R. KWOK (Jet Propulsion Laboratory, California Institute of Technology, Pasadena, California, USA)

ABSTRACT

Results of preliminary analyses of aircraft polarimetric SAR data acquired over the Greenland Ice Sheet are presented. Data were collected in August 1989 by the Jet Propulsion Laboratory (JPL) multifrequency, polarimetric SAR using the NASA DC-8 aircraft over southern Greenland. Data of this kind are the first to be acquired over an ice sheet. They are complementary to the limited coverage provided by the SEASAT satellite SAR in 1978, and more recent aircraft X-band SAR image coverage. Frequency and polarization dependencies observed in the P-, L-, and C-band image products are attributed to large-scale variations in the snow and ice surface characteristics. At this time of year, during the ablation season, ice topography exerts a strong influence upon drainage and other hydrological features on the ice sheet surface. Systematic trends in backscatter strength observed across regions of changing snow facies are suggestive of a capability to map areas of snow wetness. Trends observed at C-band indicate that algorithms could possibly be developed which have the ability to delineate areas of significant melt.

INTRODUCTION

Over the past four years, there have been several opportunities to test the utility of synthetic aperture radar (SAR) for studying polar ice sheets. Much of the interest in SAR for ice sheet studies was stimulated by data collected by the SEASAT L-band SAR which suggested the possibility for using SAR in mapping and monitoring studies. Though a limited amount of data was collected by SEASAT, it was clear that the ice margin and features of dynamic significance could be mapped. Also, the varying texture and backscatter strength indicated that the extent of different snow facies on the ice sheet could be monitored. Bindshadler and others (1987) discussed the SEASAT data along with more recently collected single-polarization X-band SAR data over northwestern and southern Greenland. They interpreted many of the features in the imagery as relating to glacial hydrology, including identifying surface lakes and stream systems. Complex mottling of the surface was interpreted as an effect associated with topographic relief, an explanation adopted by Molnia and Jones (1989) who have studied X-band airborne and SEASAT L-band SAR data collected over the Malaspina Glacier in Alaska.

In this paper, we present data collected in August 1989 over southern Greenland (Figure 1) using the JPL multichannel SAR. C-, L- and P-band data were collected at like and cross (linear) polarizations. Thus far, survey products (25 m resolution with a 4.5-km ground swath) have been produced over much of the flight tracks. A 4-look 12- X 8-km slant-range image has also been produced as a test product with a resolution of 12 m in azimuth by 7 m in range. Both the survey-processed data and the high resolution data yield images rich in texture and contrast.

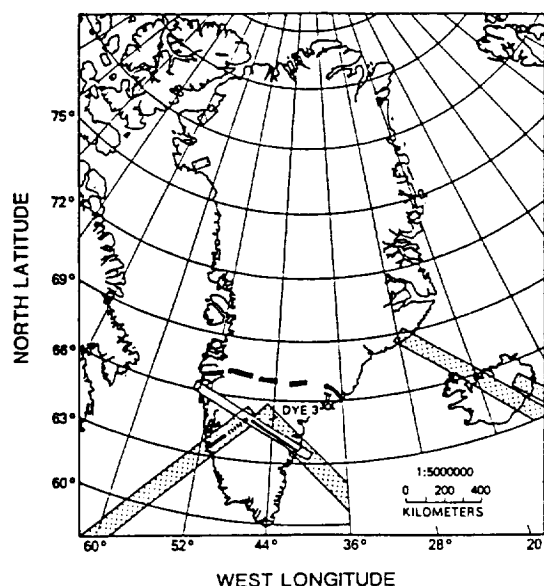


Figure 1. Map of Greenland showing areas imaged by SEASAT (stippled), airborne X-band SAR (open and hatched), the JPL multichannel SAR (heavy, dashed lines).

GLACIAL SETTING

Data discussed in this paper were collected along the heavy, dashed line in the southwestern portion of the ice sheet (Figure 1); the high resolution scene is located at the westerly end of the survey data at about 64° 30.7' N, 48° 48.7' E. Additional data were collected in 1989, but have not, as yet, been processed. The surface elevation of the most easterly point of the data set is about 2200 m. This elevation drops to about 1500 m, near the equilibrium line of the ice sheet, at the end of the processed data set. The upper layers of the ice sheet in this area have distinct morphological features that are primarily associated with the seasonal presence of free water in the snow and firn. Benson (1960) has categorized different snow facies for Greenland and a schematic diagram showing the snow facies likely to be encountered on this part of the ice sheet is shown in Figure 2. At the highest elevations, the snow is generally dry, interrupted only by intermittent ice lenses, indicative of occasional surface melt events. Descending the glacier, more ice lenses and wet snow are encountered. A water table may be present at depth. At lower elevations the water table intercepts the surface, and the snow is saturated with enough water to produce surface ponds and lakes in topographic depressions on the ice sheet surface. Free water is only present in the summer months; the effect of water is still

recorded in the glacier during the winter by the amount of ice lenses present in the region of the glacier where net accumulation has occurred, and by the amount of hard ice in the lower ablation areas of the ice sheet, which may be covered by a veneer of snow in winter.

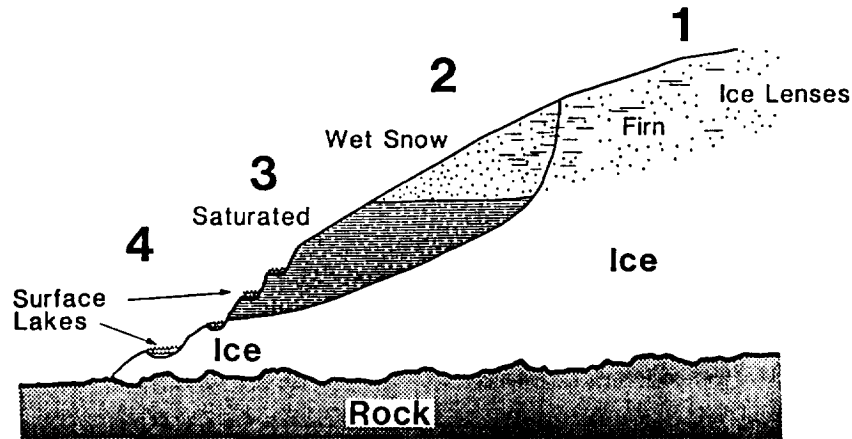


Figure 2. Schematic representation of different snow facies present on the Greenland Ice Sheet.

SAR DATA

Survey data illustrates the individual channel responses of C-, L- and P-bands at HH, VV, and HV linear polarizations. Upon examining the principal components of the data set, it was apparent that polarimetric information contained within a single frequency is correlated, and furthermore, that the main source of variation in this nine-channel data set was between the different frequencies used. Thus, before proceeding further in the analysis, the individual polarization channels for each frequency were averaged to reduce speckle. Results for the C-, L-, and P-band survey data are shown in Figure 3. A scene of full resolution data was also processed. The C- and P-band data for this scene are shown in Figure 4.

There is little detail present in the survey data (Figure 3) over the highest elevations (top of the three left strips) of the flight line. This situation changes at lower elevations where there are complex intensity patterns evident on all channels. Based on previous experience with STAR-1 INTERA X-band and SEASAT L-band SAR data collected in the same general vicinity, we suspect that many of the most prominent features are related to glacier lake and stream systems. One unexpected outcome of the multifrequency imaging is the large areas of contrast reversal, especially between P- and C-band. Areas of contrast reversal are very evident in the high resolution data. As described later, we suspect these are related to frequency-dependent penetration depths and important morphologic differences between the near surface and deeper snow and firn.

Figure 4 shows two color-classified polarimetric total power images of the same area taken from the strip in Figure 3 at C- and P-band. Each polarization combination is

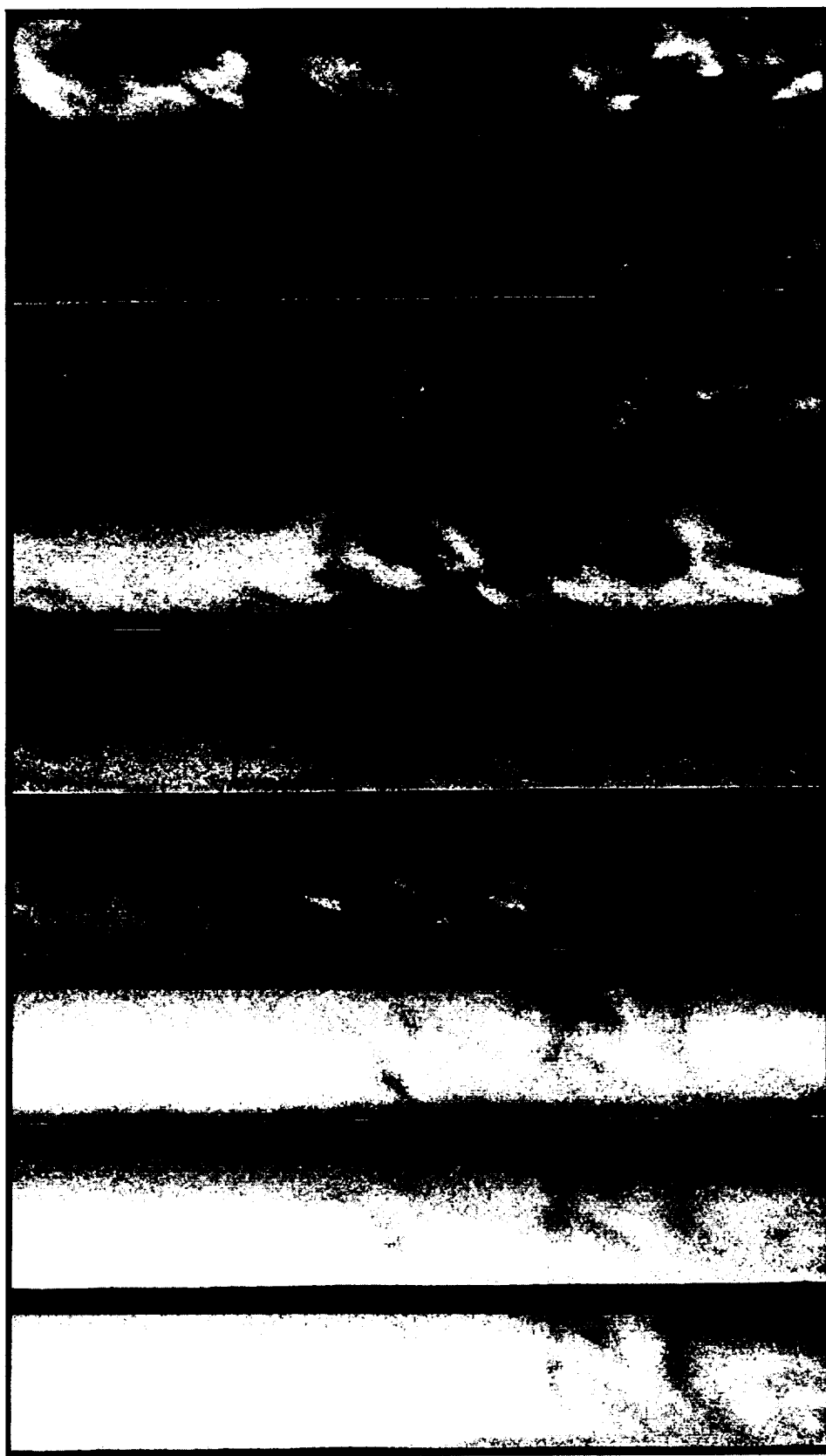


Figure 3. C-, L- and P-band survey data averaged over each polarization to reduce speckle. Three groups of C-, L- and P-band data are shown for comparison of the different frequency data. Highest elevation is at the top of the first three strips. Lowest elevation is at the bottom of the final three strips.

overlaid on the intensity image as a color, where the two linear copolarizations (HH and VV) are denoted by red and green, and linear cross-polarization (HV) by blue. The resulting neutral hues and the lack of any predominant color saturation in this scene confirm that little independent information is contained in the amplitudes recorded at the various polarization combinations. However, this in itself is an important observation, since it requires that the mechanisms of scattering be limited to combinations of geometric optics and volume scattering. Another observation from Figure 4 is that surface, or perhaps subsurface, crevasses are more clearly observed at P-band than at C-band. Those areas identified as having extensive systems of fractures at P-band are in many instances obscured in the C-band image due to contrast reversal. This may be because the P-band has the ability to 'see' deeper into the firn, whereas the C-band energy is absorbed before it penetrates deep enough to image deep crevasses. This is borne out by the fact that areas of crevasses which can be observed at C- and P-bands also tend to be bright at both frequencies.

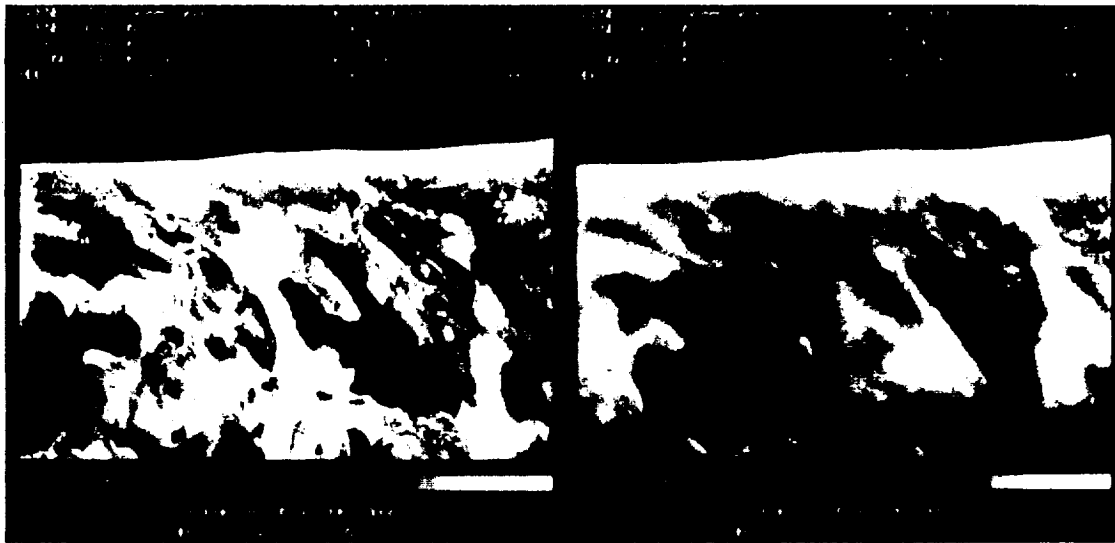


Figure 4. C- and P-band full resolution data. Polarization data are coded by color.

To simplify data interpretation, a 10-pixel swath along the centerline of the survey data was selected and the pixels averaged together. Data values produced down the length of each data strip are shown as the profiles in Figures 5, 6, and 7. Figure 5 shows the profiles for the C-band, like polarized channels. Immediately obvious is the high value of relative pixel intensity at high elevations followed by a sloping ramp down towards a plateau of low values of relative pixel intensity at low elevation. Referring to Figure 2, this intensity signature is believed to be characteristic of snow facies changing from mostly dry to wet and saturated snow. Pixel intensities are high in the dry snow regime

where volume scatter dominates the signal. As the snow wetness increases, penetration decreases while forward scatter increases, causing a net decrease in pixel intensity until the point where the snow is fully saturated with water. C-band data demonstrate the greatest relative dynamic range, falling by 10 dB down the profile line. The L- and P-bands demonstrate a relatively smaller dynamic range, the mean intensity values dropping by only 4 dB along the profile.

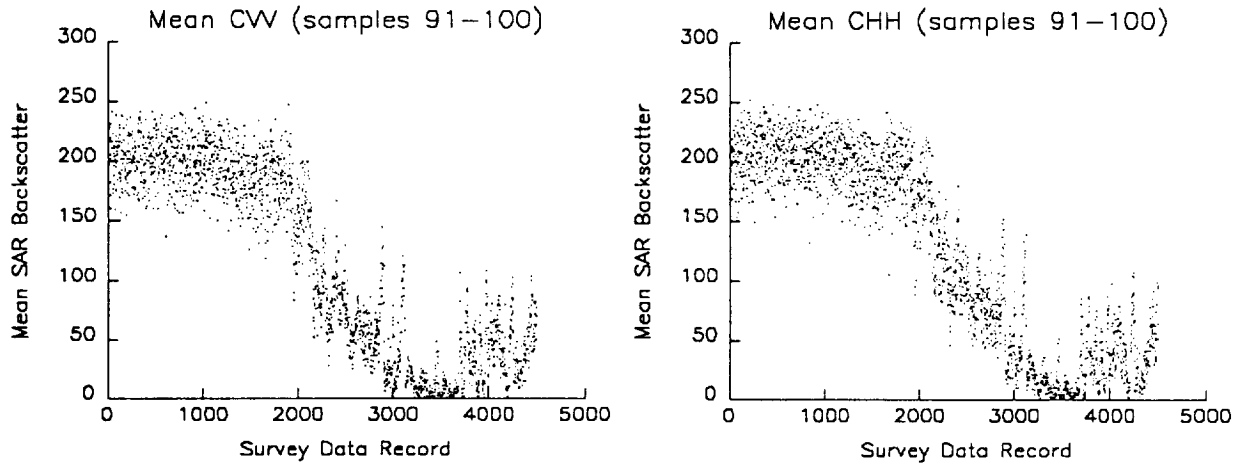


Figure 5. Profile of the mean of 10 pixels located in the center of the C-band imagery down the flight line. Upper profile shows VV data; lower profile shows HH data.

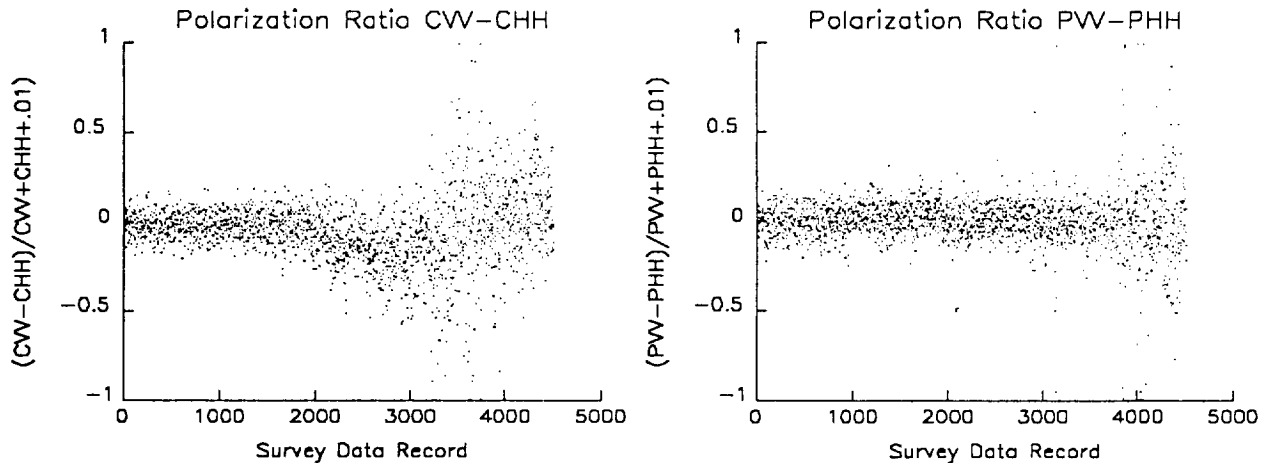


Figure 6. Profile of the polarization ratio for 10-pixel means, calculated by taking the quotient of the difference between VV and HH channels and dividing by their sum. Upper plot shows polarization ratios for the C-band data; lower plot shows P-band polarization ratios.

Penetration into the dry snow and volume effects cause the like polarization channels to behave similarly, as seen in Figure 6 where polarization ratios are plotted. The P-band polarization record is nearly constant in magnitude (nearly zero mean) and variability across the entire data set, supporting the contention that volume scattering and

geometrical optics effects are the dominant scattering mechanisms. C-band polarization behaves similarly through the midpoint of the data set. There is a subsequent drop in polarization followed by increasing polarization and variability. These later observations suggest that surface scatter may become important in the saturated snow and ablation facies.

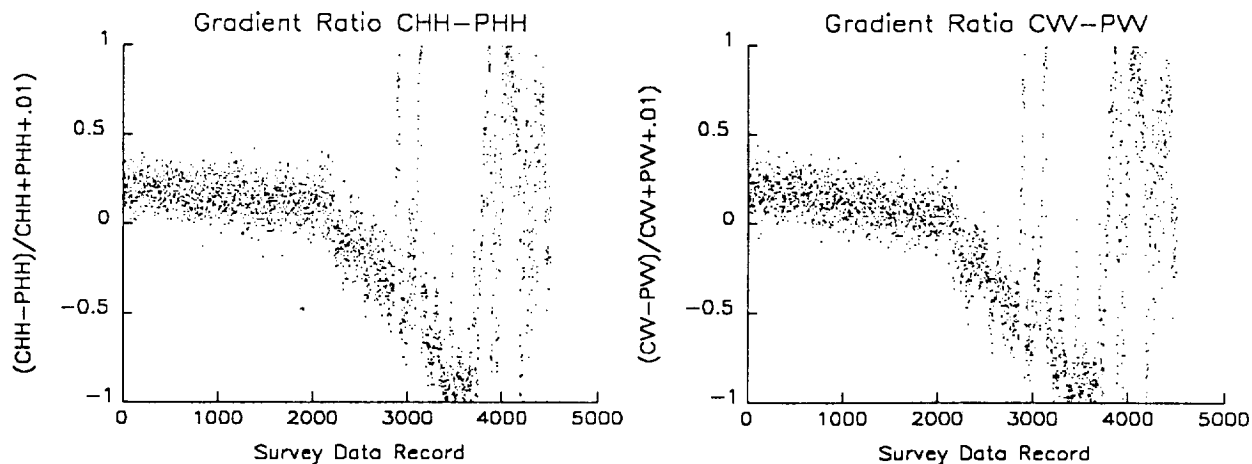


Figure 7. Gradient ratio for 10 pixel average profiles calculated by taking the quotient of the difference of C-band and P-band like polarization channels and dividing by the sum. Upper profile shows gradients for the H channels; lower profile shows gradients for the V channels.

Intensity differences between each frequency channel account for the shape of the gradient ratio curves shown in Figure 7. At the higher elevation, relatively drier snow regions, C-band intensities are greater than P-band which we interpret as a consequence of increased Rayleigh scattering by snow grains for the shorter wavelength ($\lambda = 5.6$ cm) channel. At lower elevations, the P-band data dominate. We attribute this to the much reduced penetration depth into the wet snow at C-band and the increase in forward scatter away from the radar. The P-band signal continues to penetrate, and volume scatter, probably from buried ice lenses, still contributes to the return signal. The more limited effect of snow wetness on the P-band data relative to the C-band data is supported by trends in data presented by Stiles and Ulaby (1980). Those authors show that there is about a 5 dB difference in backscattering strength between wet snow and dry snow at C-band and at a viewing angle of 50° . The difference between the backscattering coefficient for wet and dry snow at P-band is less than 1 dB.

Finally, note that the broad trends in the profiles shown in Figures 5, 6, and 7 are interrupted at the lower elevations by large spikes. We believe these spikes correspond to the locations of surface lakes. It is clear from the gradient ratio profile that the C-band and P-band data are responding very differently in these areas and indeed many of the bright spikes in C-band are dark areas in P-band. We offer the following speculation that perhaps some of the lakes have already begun to freeze over. Thin snow cover, air bubbles, or fractures in the ice cover may be sufficient to cause backscatter at C-band, but the density or size of the inhomogeneities is insufficient to cause important scatter at P-band.

CONCLUSIONS

Multichannel SAR yields texturally rich images of the Greenland ice sheet. Qualitative analysis of the data suggests that characteristic trends in the data may be related to the degree of snow wetness. The pattern of a high intensity plateau followed by a downsloping ramp and terminating in a flat, low intensity plateau are strongest at C-band. The simplicity of the pattern suggests that it may be feasible to construct an algorithm for mapping these regions using more extensive satellite SAR data.

REFERENCES

- Benson, C. S., 1961. Stratigraphic studies in the snow and firn of the Greenland Ice Sheet. *Folia Geographica Danica*, vol. 9, p. 13 - 38.
- Bindschadler, R. A., K. C. Jezek and J. Crawford, 1987. Glaciological investigations using the synthetic aperture radar imaging system. *Annals of Glac.*, no. 9, p. 11-19.
- Molnia, B. F., and J. E. Jones, 1989. View through ice. *EOS*, vol. 70, no. 28, p.701, 710.
- Stiles, W. H., and F. T. Ulaby, 1980. Microwave Remote Sensing of Snowpacks. NASA Contractor Report 3263, p. 404.

COMPARISON OF ACTIVE AND PASSIVE MICROWAVE SIGNATURES OF ARCTIC SEA ICE

DRINKWATER, M. R., and J. P. CRAWFORD (Jet Propulsion Laboratory, California Institute of Technology, Pasadena, CA, USA)

CAVALIERI, D. J. (NASA Goddard Space Flight Center, Greenbelt, MD, USA)

HOLT, B., and F. D. CARSEY (Jet Propulsion Laboratory, California Institute of Technology, Pasadena, CA, USA)

ABSTRACT

In March 1988, overlapping active and passive microwave instrument data were acquired over Arctic sea ice using the NASA DC-8 aircraft equipped with multifrequency, variable polarization SAR and radiometer. Flights were conducted as a series of coordinated underflights of the DMSP SSM/I satellite radiometer in order to validate ice products derived from the SSM/I radiances. Subsequent flights by an NRL P-3 aircraft enabled overlapping high-resolution, single frequency image data to be acquired over the same regions using a Ka-band scanning microwave radiometer. In this paper, techniques are discussed for the accurate coregistration of the three aircraft datasets. Precise coregistration to an accuracy of $100 \text{ m} \pm 25 \text{ m}$ has, for the first time, enabled the detailed comparison of temporally and spatially coincident active and passive airborne microwave datasets. Preliminary results from the intercomparisons indicate that the SAR has highly frequency- and polarization-dependent signatures, which at 5.3 GHz (C-band) show an extremely high correlation with the 37 GHz radiometric temperatures.

INTRODUCTION

During March 1988, the NASA DC-8 aircraft collected extensive active and passive microwave data over the Beaufort, Bering, and Chukchi Seas in support of NASA's SSM/I validation program (Cavalieri, 1988). In total, fifteen flights were conducted by two Navy P-3's and the NASA DC-8 as part of this validation effort. Arctic regions overflown by the NASA and Navy aircraft are displayed in Figure 1. A full summary of these flights is available in Cavalieri et al. (1990) along with dates, locations, concurrent satellite coverage (by SSM/I, NOAA-9 and 10, and LANDSAT 4 and 5) and results from data intercomparison and validation efforts.

The DC-8 was equipped with both the Jet Propulsion Laboratory (JPL) multifrequency, polarimetric Synthetic Aperture Radar (SAR), and the Goddard Space Flight Center (GSFC) Airborne Multifrequency Microwave Radiometer (AMMR). These flights were unique in that, for the first time, both SAR and AMMR sea ice datasets were obtained concurrently from the same platform. The fixed-beam AMMR antennas were configured to record brightness temperatures inside the SAR swath at 45° incidence. A precision collocation exercise was undertaken during data postprocessing by incorporating aircraft attitude information from the Inertial Navigation System (INS). This enables registration of each AMMR instantaneous field-of-view (IFOV) to known SAR pixel locations. In addition, digital radiometric data acquired by a mapping radiometer on the NRL P-3 have been registered with these DC-8 data for further comparisons.

INSTRUMENTATION

The left-looking JPL SAR operates at 0.4, 1.25, and 5.3 GHz ($\lambda = 5.6, 24,$ and 68 cm) simultaneously, transmitting and receiving from separate antennas at HH, HV, VV, and VH linear polarization combinations and digitally recording the amplitude and relative phases of the scattered wave. Unlike previous conventional monostatic imaging radars, this system enables the full scattering matrix to be recorded. This permits the backscattering coefficient to be synthesized for a specified transmit and receive polarization, at any of the three frequencies used. The incidence angle varies from 30 to 55° within a scene and the swath width of the instrument is approximately 10 km in slant range. The resolution varies between 26 m (survey) and 12 m (high resolution) depending on the processing used.

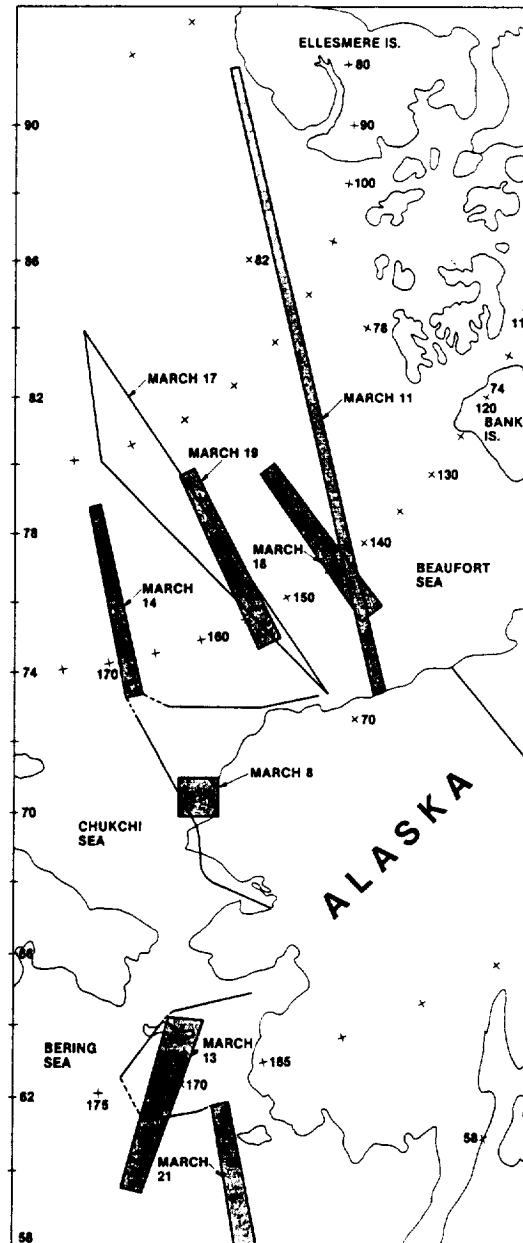


Figure 1. Map of areas covered by the NASA DC-8 aircraft remote sensing flights during the SSM/I validation campaign in March 1988.

Goddard Space Flight Center (GSFC) supplied the AMMR sensor, which closely matches the SSM/I radiometer frequencies and polarizations. The AMMR records radiances using several fixed-beam, dual polarized antennas receiving 18, 21, 37, and 92 GHz frequencies ($\lambda = 1.67, 1.43, 0.81, \text{ and } 0.33 \text{ cm}$). During the campaign, each antenna aperture was configured to look at 45° incidence (to the left of the aircraft) along the center of the SAR swath.

The DC-8 flights were coordinated with an NRL P-3 aircraft which carried the NORDA Ka-band Radiometer Mapping System (KRMS), operating at 33.6 GHz. This high resolution (100 m) imaging system provided complementary brightness temperature maps illustrating the variability of the emissivity and surface radiometric temperature of the ice being observed by the AMMR and SSM/I sensors. Flight lines were chosen so as to image sea ice areas previously observed by the SAR and AMMR. Precise replications of the DC-8 flight lines have enabled the KRMS images to be accurately overlaid upon the SAR and AMMR data.

DATA REGISTRATION AND CLASSIFICATION

Collocation of the DC-8 active and passive microwave datasets was made possible by indexing the SAR and AMMR data streams with the current aircraft time indicated by the DC-8 housekeeping system. Every second, this system routinely records all pertinent instrument and aircraft parameters including INS navigation, ground speed, and universal time, thus enabling cross-comparisons of data and aircraft parameters.

To account for changes in aircraft ground speed in the AMMR along-track data (non-motion compensated), INS, universal time, and radar configuration parameters were recovered for 5 records, each separated by 3-minute intervals, along 15-minute radar image segments. These equally spaced control points were subsequently used to match the data streams by interpolating the location of the remaining AMMR measurements with respect to the motion-compensated SAR data records. The result is that each AMMR data point was matched with every 9th or 10th SAR record, depending on the ground speed of the aircraft. At typical ground speeds of 200 ms^{-1} or more, the accuracy of the coregistration is determined by the AMMR beam width and the integration period (1.0 s). From crossings of distinctive targets in the SAR images, it is clear that the two data sets are registered to within an accuracy of several SAR pixels (or 0.5 s along-track delay). This translates to a locational accuracy of $100 \text{ m} \pm 25 \text{ m}$.

For the purposes of this study, 26 m resolution survey processed data were used since these provided contiguous strips of SAR image data up to 200 km in length. C-band VV-polarization SAR data are chosen here for display products largely because they provide good contrast between first-year and multiyear sea ice classes. Figure 2 illustrates the result of coregistering the AMMR instantaneous field of view (IFOV) with the SAR image. Only a narrow portion of the total SAR swath is displayed, within which the aircraft roll-determined position of the IFOV is indicated. Figure 2 is a typical segment of C-band VV SAR data (for display it is split into columns) collected over the Beaufort Sea first-year/multiyear ice transition zone. Monochrome strips represent a grey level rendition of SAR relative backscatter magnitude in which light tones correspond to multiyear ice and dark tones to first-year ice. Corresponding color-coded strips are the result of a clustering algorithm which separates first-year ice (blue) from multiyear ice (red) in the C-band data. SAR pixels corresponding to the center of the AMMR IFOV are located inside the SAR swath. These points are represented by "+" characters on both the original (black and white) and clustered (color) images. Dashed lines located along either side of the center points correspond to the limits of the 3 dB footprint for each integration period, as represented by the AMMR 37 GHz antenna pattern. Values indicated between the corresponding color and black and white image strips represent the 37 GHz brightness temperatures for each AMMR one-second integration period. Zero values indicate instrument calibration cycles (approximately every 60 seconds).

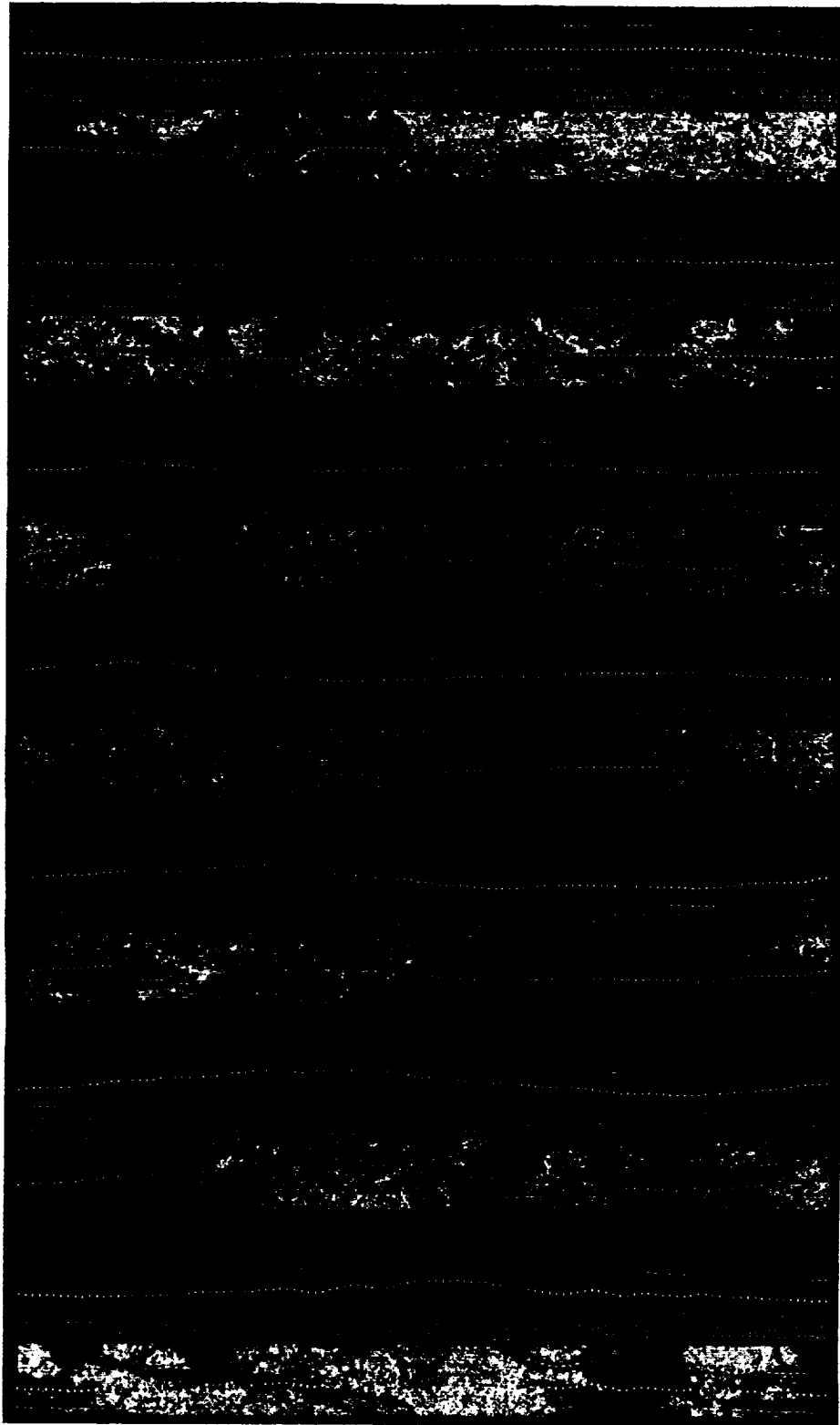


Figure 2. JPL SAR strip images for a portion of the March 11 Beaufort Sea flight track illustrated in Figure 1. Small crosses indicate the position of the center of the AMMR footprint and the numerical value at right of each monochrome strip is the brightness temperature times ten for the 37 GHz V-polarization channel. Colour-classified versions of the SAR image strips are plotted alongside, indicating multiyear ice and first-year ice as red and blue, respectively.

The technique used to obtain accurate classification of ice types in the SAR data involves two procedural levels. The first stage involves smoothing the image using a 3 x 3 moving box filter to reduce image speckle, and then applying an unsupervised Bayes classifier to separate recognizable subcategories of first-year and multiyear ice. In the second stage of processing a supervised Bayes maximum likelihood classifier was employed, based on the assumed knowledge of the probability distributions over the range of classes and the known cluster centers. The resulting classification into multiyear and first-year ice is based upon minimum distance of each image pixel to the cluster centers. This operation is carried out on a pixel-by-pixel basis, resulting in multiyear ice pixels coded red and first-year ice pixels coded blue. Similar SAR ice classification techniques have been developed to generate ice classification images, in an automated fashion, using ERS-1 images received at the Alaska SAR Facility. Holt et al. (1989) employed a comparable Bayes maximum likelihood method and compared their classification results with aerial photographic and KRMS image data. This comparison indicates 3 to 7% accuracy for first-year or multiyear ice concentration estimates from the C-band VV-polarized aircraft SAR data.

KRMS data were digitally coregistered with the SAR data, using visual tie-points chosen from features recognizable in both image strips. Some several hundred points were used for each image strip, and the computer collocation procedure was achieved by 'rubber-sheeting' the KRMS image (courtesy of D. Eppler, NOARL) onto the SAR strips. This also enabled the intercomparison of the KRMS (NRL P3) and the AMMR data (DC-8), since the precise location of the AMMR values, with respect to the SAR, was known. One example of the results taken from the 11 March flight data is shown in Figure 3 (from Cavalieri et al. 1990). The resulting rotation and stretching or compression of the KRMS imagery is most evident at the top of the radiometer image panel in Figure 3.

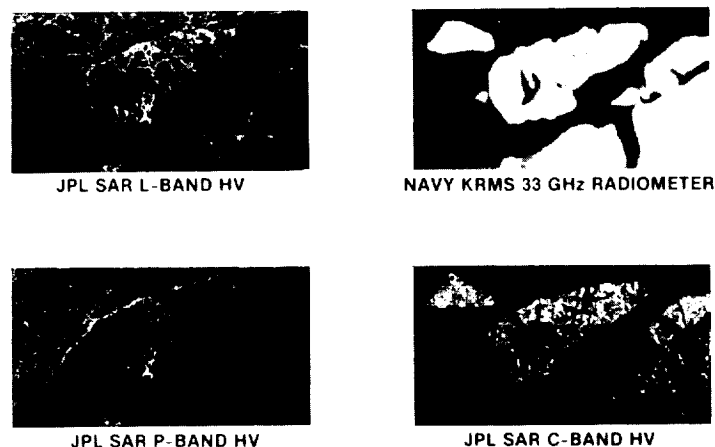


Figure 3. Comparison of digitally coregistered SAR and KRMS image data taken from the 11 March flights of the DC-8 and the NRL P-3. Radiometrically 'cold' targets appear as white in the KRMS images, and light grey in the C-band cross-polarized panel. P- and L-band SAR panels illustrate the capability at lower frequencies to distinguish areas of ridging or internal deformation (from Cavalieri et al. 1990).

ACTIVE-PASSIVE DATA COMPARISON

This coregistration is providing the first accurate high resolution comparison of active and passive microwave data sets over Arctic sea ice. Preliminary results comparing C-band SAR with 37 GHz AMMR data from the Beaufort Sea show an extremely strong inverse correlation across the first-year to multiyear ice transition zone. Figure 4 shows a scattergram and regression of 5.3 GHz HV-polarized mean SAR pixel values (i.e. relative backscatter magnitude in dB) and AMMR brightness temperatures (in Kelvins) from the IFOV of the 37 GHz V-pol antenna. The regression indicates a correlation of $R = -0.94$, and the relative backscatter coefficient decreases monotonically as the 37 GHz brightness temperature increases. Bright cross-polarized C-band radar signatures, associated with low salinity multiyear ice (diamond symbols > 95% multiyear ice), correspond with low brightness temperatures (190 to 200 K), probably due to volume scattering within the old ice. Multiple scatter caused by air inclusions contributes to the high cross-polarized signal observed. The mechanism causing lower brightness temperatures for multiyear ice is the lower emissivity due to the lower salinity and the scattering caused by air inclusions or bubbles in the freeboard layer of the ice. In contrast, low backscatter from young and smooth first year ice is linked to high brightness temperatures (triangle symbols represent 100% thick first-year ice). For these higher salinity ice forms, the optical depth is less than one wavelength, so the relevant microwave emission is derived predominantly from the ice within a shallow depth of the surface. This remains true even with a snowcover, as long as the snow is dry, fine, non-saline and of shallow depth.

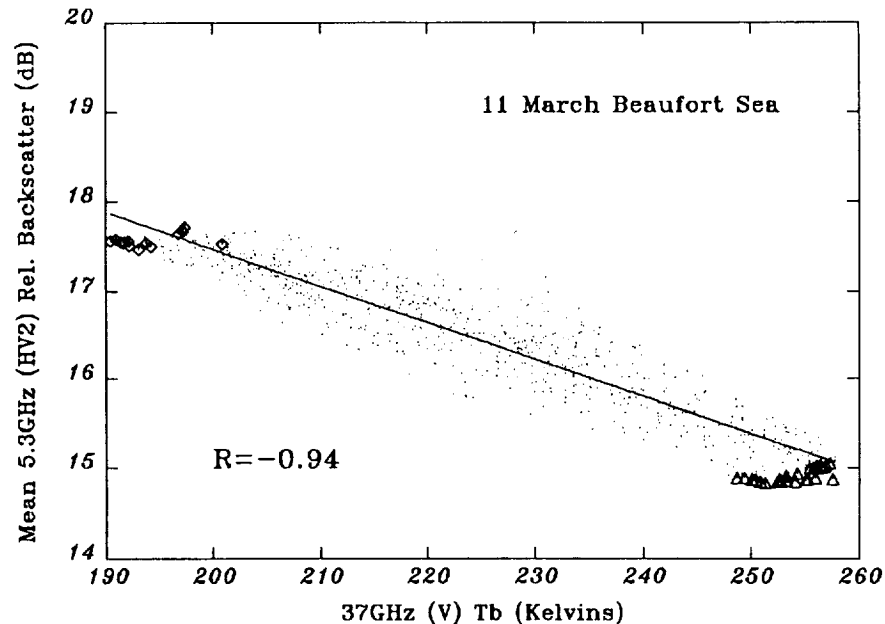


Figure 4. Scattergram and regression of 37 GHz AMMR brightness temperatures and Mean C-band HV-polarized relative SAR backscatter. The correlation coefficient between the two parameters is -0.94. Triangles at the warmer brightness temperatures indicate areas of 100% first-year ice, and the diamonds indicate areas with over 95% multiyear ice.

An important observation from Figure 4 is that there is almost a perfect linear relationship between the two variables. The example noted occurs only for situations in which the total ice concentration is 100%, and thus in all cases there is no open water in the footprint of the AMMR. The brightness temperature recorded by the radiometer is thus confirmed to be a simple linear function of the proportions of warm and cold targets within the footprint.

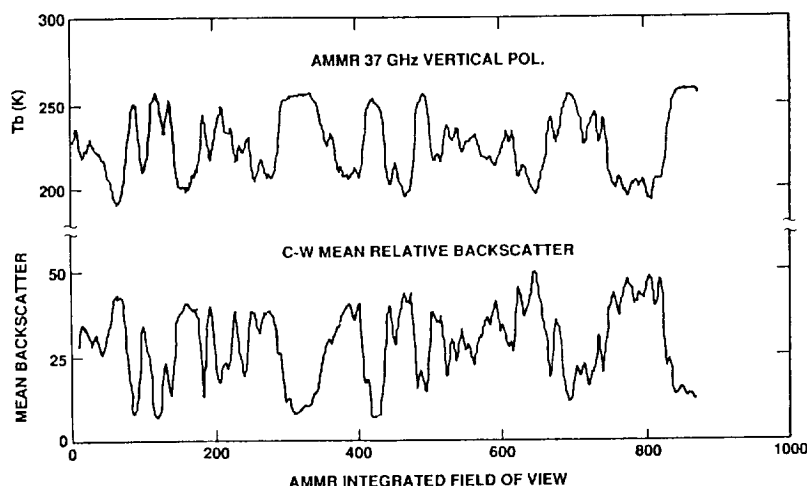


Figure 5. Comparison of along-track values of C-band VV-pol SAR backscatter and 37 GHz V-pol AMMR brightness temperatures; data correspond to the coregistered data set shown in Figure 2.

Figure 5 indicates the along-track variability in the AMMR brightness temperatures in conjunction with the mean SAR backscatter statistics. This 170 km section of data corresponds with the strip of survey data shown in Figure 2. The large areas of smooth, thick, first-year ice which separate multiyear ice floes in this region result in peaks in brightness temperature tending to 250 K or more. Multiyear floes demonstrate values in the troughs which tend to 200 K or less. Small-scale fluctuations in the lines indicate variability in the surface properties of the ice forms and also reflect the complex mixtures of first-year and multiyear ice types which are present in this region.

DISCUSSION

It is evident from these results that spatially coregistered active and passive microwave data will lead to greater flexibility and reduced ambiguity in our discriminatory capability with sea ice. It is now necessary to investigate the variability in the signatures from a multifrequency and polarimetric perspective. Eigenvector or principal component analysis will enable us to see how many of the channels possess independent information and which combination gives us the greatest discriminatory capability. This is especially important in the context of future Eos-type satellite radar and radiometer systems.

Preliminary results using purely spectral information appear to enable discrimination with reasonable success, as is shown in Figure 6. This figure shows a scatter plot of values from a dimensionless ratio of textural statistics extracted from the C- and P-band SAR data (by *mean* backscatter and standard deviation *sig*) compared with spectral gradient ratio information provided by an algorithm similar to that currently used for ice classification in SSM/I data. The feature space defined by these variables shows good separation between multiyear ice and first-year sea ice. Radiometer footprints which have over 90% multiyear ice are denoted by triangles. The AMMR spectral gradient ratio extracted for these areas is negative due to the fact that the brightness temperature at 37 GHz V-pol is lower than that at 18 GHz. The corresponding high variance or texture in the multiyear ice returns leads to small SAR spectral ratios of around 0.5. Thus areas of multiyear ice are well discriminated from the contrasting areas of thick first-year ice (denoted by diamonds). With examples from 97 to 100% first-year ice, the difference between 37 and 18 GHz radiometric temperatures is small and values for the AMMR gradient ratio cluster around 0.0. In both C- and P-bands these areas are relatively textureless and the resulting SAR spectral ratio increases to values of 1.5 or more.

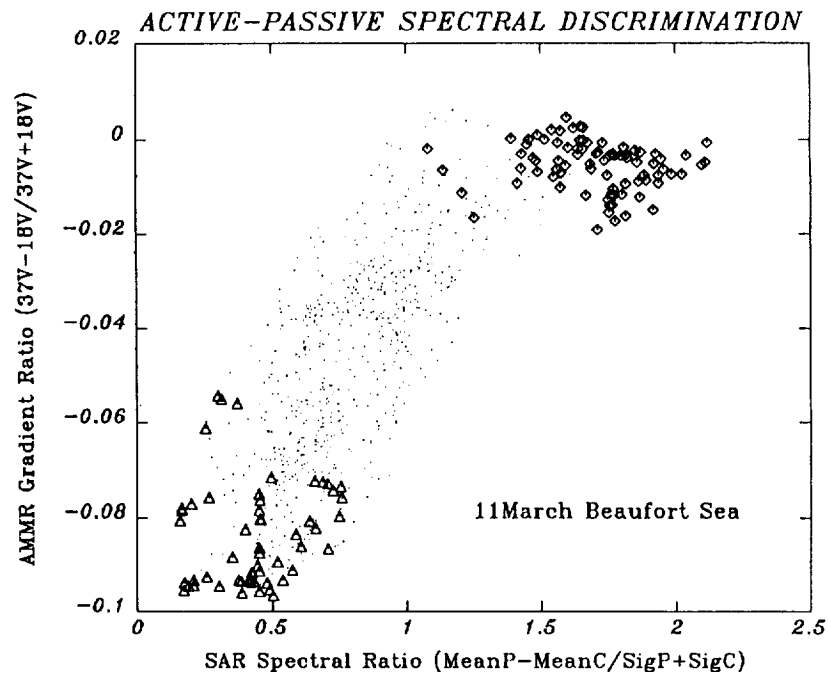


Figure 6. Scattergram indicating microwave discrimination of first-year and multiyear ice on the basis of spectral gradients in the AMMR data and spectral gradient and texture statistics from the SAR relative backscatter image. Triangles indicate footprints of >90% multiyear ice, and diamonds >97% first-year ice. Intermediate mixtures are denoted by single points.

Intermediate mixtures of first-year and multiyear ice in this 11 March Beaufort Sea example fall along a curve indicated by the points plotted in the feature space.

In conclusion, combinations of active and passive microwave data from future multi-sensor satellite platforms such as Eos will lead to an increased capability to extract sea ice geophysical information, in order to study the delicate balance and interactions between the cryosphere, atmosphere, and hydrosphere.

ACKNOWLEDGMENTS

The authors thank the flight crews of the NASA DC-8 and NRL P-3 for their skills in data acquisition, and the Radar Sciences group at JPL for data processing. We are also grateful to Duane Eppler of NOARL for contributing the KRMS radiometric images used in this study. This work was performed under contract to NASA at the Jet Propulsion Laboratory, California Institute of Technology.

REFERENCES

- Cavalieri, D. J., 1988, NASA sea ice and snow validation program for the DMSP SSM/I: NASA DC-8 flight report, NASA Technical Memorandum, 100706, September 1988.
- Cavalieri, D. J., J. P. Crawford, M. R. Drinkwater, D. T. Eppler, and L. D. Farmer, 1990, SSM/I aircraft underflights: introduction and aircraft sensor intercomparisons, In Cavalieri, D. J. et al. (Ed.), NASA DMSP SSM/I Sea Ice Validation Program Final Report, Chapt. 7, NASA Technical Memorandum, In Press.
- Holt, B., R. Kwok, and E. Rignot, 1989, Ice classification algorithm development and verification for the Alaska SAR facility using aircraft imagery, Proceedings of IGARSS '89, Vol. 2, p. 751-754.

7
p-6

RIVER AND LAKE ICE CONDITIONS AS DETERMINED FROM AIRSAR IMAGERY

RAE A. MELLOH and LAWRENCE W. GATTO,
U.S. Army Cold Regions Research and Engineering Laboratory
Hanover, New Hampshire 03755

ABSTRACT

Synthetic aperture radar (SAR) imagery data can provide information on types and distribution of river and lake ice needed for studying river ice processes and dynamics, monitoring ice during winter navigation, and formulating ice control strategies. Visible and IR remote sensing systems cannot provide such data and present field methods are inadequate for characterizing ice conditions over long river reaches. Our ongoing analysis of JPL's AIRSAR imagery data and concurrent ground truth of ice conditions on the Tanana River and surrounding lakes near Fairbanks, Alaska, in March 1988, has resulted in several findings: hummocked ice covers and zones of variable ice surface roughness within them can be differentiated; C- and L-band data are more sensitive than P-band to the range of surface roughnesses encountered; smooth, level ice that is clear or contains small bubbles produces little backscatter; snow-covered river ice, whether rough or smooth, is distinguishable from snow-covered river sediments on exposed river beds and unvegetated bars; and open water leads are readily distinguished.

INTRODUCTION

During March 1988, an opportunity arose to collect ground verification of river and lake ice types and conditions in the Tanana River Valley near Fairbanks, Alaska, coincident with overflights of the NASA/JPL Airborne Synthetic Aperture Radar (SAR). Our general hypothesis was that variations in surface roughness, volume inhomogeneities and dielectric discontinuities between air, snow, ice and water layers would affect the strength of radar backscatter, allowing the interpretation of river ice types and distribution. Previous studies including those by Page and Ramseier (1975), Bryan and Larson (1975), and Weeks et al. (1978) have suggested the use of radar in freshwater ice environments. This investigation seeks to develop an understanding of the characteristics of river and lake ice that produce SAR image patterns.

CRREL field teams obtained extensive ground and aerial observations and measurements at a variety of river and lake sites (Fig. 1). The ground truth data includes aerial videotape, observations of snow depth and stratigraphy, ice core descriptions and thickness measurements, surface roughness measurements, noncontact magnetic induction surveys and impulse radar traces.

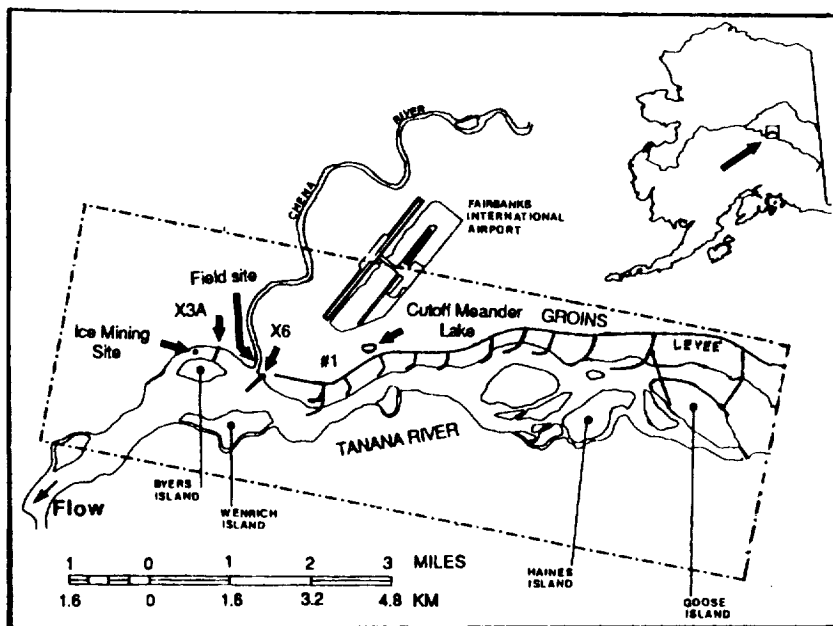


Fig. 1.
Location map.

Uncalibrated AIRSAR images acquired on March 13 and 19 (when air temperatures were above and below freezing, respectively) are compared with our ground observations. The angles of incidence for most features of interest were between 40° and 50° . The flight altitudes were around 8900 m and data were collected at P-, L- and C-bands (.45, 1.26, 5.3 GHz, respectively).

RESULTS TO DATE

River Patterns

Ice jams : The most obvious patterns on the Tanana River SAR images (Fig. 2) are the light (high backscatter) reaches interspersed with reaches of intermediate and dark tones (low backscatter). The light areas correspond to ice floe accumulations that developed during freeze-up; we refer to these congealed accumulations as ice jams. Typical root-mean-square roughnesses in the jams were 4 cm for the snow surface and 10 cm for the top ice surface. Over the winter, ice thickening due to thermal growth of columnar ice or freezing of frazil deposits may have lessened the roughness of the bottom ice surface relative to the top. Both surfaces may contribute to increased backscatter from the ice jams, though the bottom surface provides the greater dielectric contrast and, hence, greater reflectivity.

Within the jams shown on the images, the lightest portion is the downstream end, which corresponds to the area with the largest surface relief and thus highest backscatter. Root-mean-square roughness measurements at the downstream end of the ice jam at Groin #1 were 7 cm for the snow and 19 cm for the top ice surface. The tone darkens in the upstream direction because the surface roughness and relief within the jams typically decrease upstream, resulting in less backscatter.

The longitudinal, linear, light pattern within the jams (Fig. 2) probably delineates the main flow channel below the ice cover. The ice



Fig. 2. NASA/JPL AIRSAR image, March 13, 1988; ice jams and longitudinal patterns (1), smooth river ice (2), smooth lake ice (3), brash ice (4), open lead (5), river bed and bars (6), vegetated islands (7).

surface here may be rougher than along the channel margins because of higher forces in the middle of the channel, resulting in thicker and rougher accumulations. A less rough border ice may have already formed near the banks. Ground electrical conductivity measurements we made with the magnetic induction instrument (Arcone et al. 1987) across the river channel at the Groin #1 and X6 sites (Fig. 1) suggest that the main channel is in the location indicated by the light patterns.

Ice thickness in the smooth ice section downstream of the jam at Groin #1 ranged from 51 to 76 cm and consisted predominantly of columnar ice over congealed frazil. The smooth ice downstream of the Tanana and Chena River confluence ranged from 35 to 69 cm and consisted primarily of columnar ice. Thicknesses of the rough ice at the Groin #1 site, which consisted of congealed frazil with some columnar ice, ranged from 99 to 112 cm. With the exception of a few centimeters of snow ice at the top, the bubble content of the ice was low and bubble sizes were in the 1- to 4-mm range.

Smooth ice : Dark image patterns (low backscatter) within the rivers are formed by unjammed ice with a smooth, level surface such as at the X3 and Groin #1 sites on the Tanana and Chena Rivers (Fig. 2).

Many of the lakes adjacent to the Tanana and Chena Rivers occur in old gravel borrow pits and have surface areas of less than 10 acres. Most of these lakes appear dark on the SAR images (Fig. 2). Ice cores taken in a small lake ranged between 13.5 and 56.0 cm in thickness and consisted of less than 10 cm of snow ice and bubbly ice at the top with columnar ice below. The ice surface typically was smooth and the snow above on most of the lake was compacted by snowmobile passes. The small lake is difficult to discern from the surrounding abandoned river bed.

Open water : A dark linear pattern (low backscatter) within the Tanana River (Fig. 2) corresponds to an open water lead. Open leads

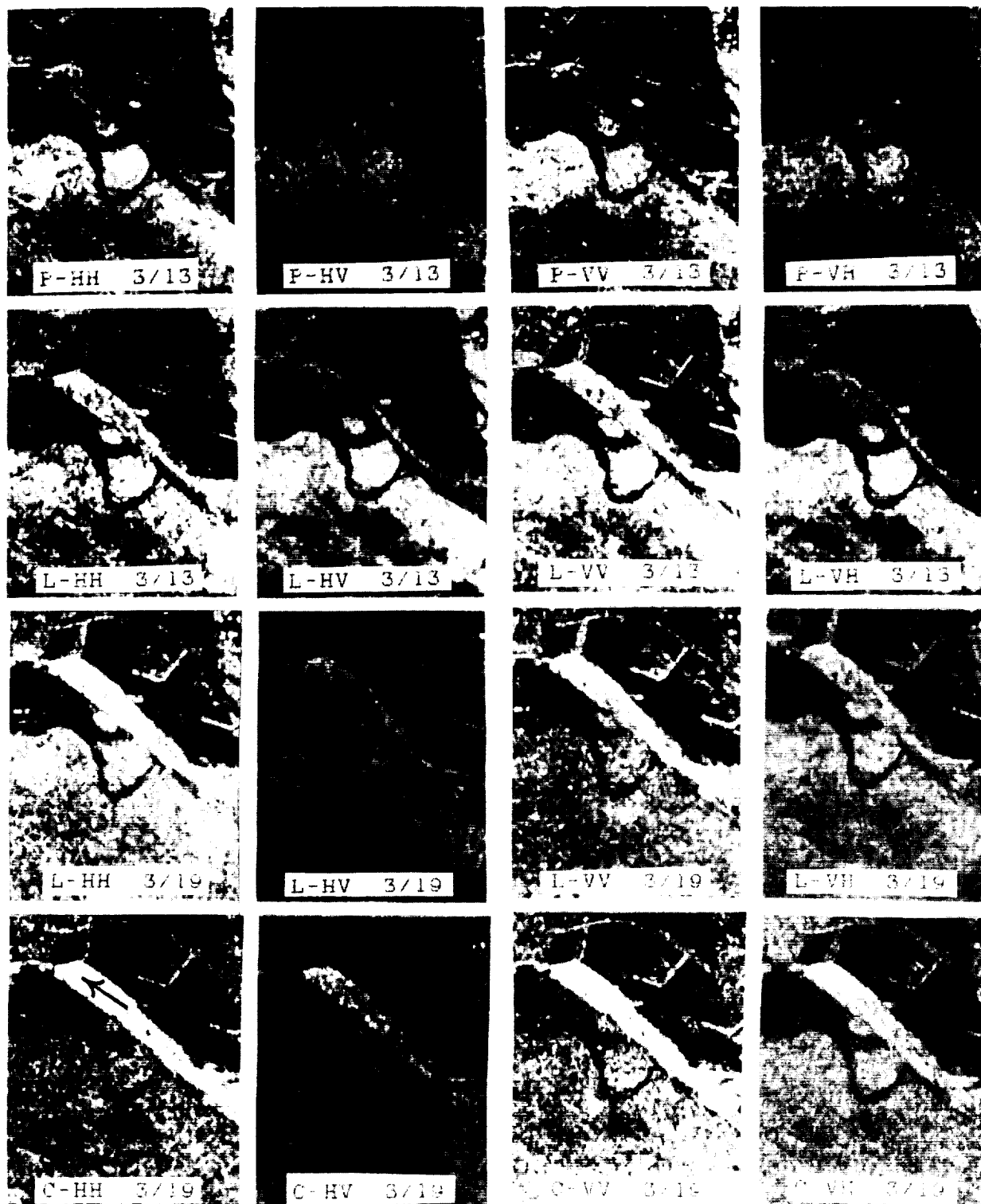


Fig. 3. Single band co- and cross-polarization images of the ice jam at Groin #1, on March 13 (P,L) and March 19 (L,C). The arrow on the bottom left photo indicates the location of the jam and the direction of river flow.

were observed at numerous points along the river during the aerial reconnaissance.

Snow : Although the snow was substantially wetter on 13 March than on 19 March, differences in the snow patterns on the images are subtle. Channel patterns and drainage ways in undeveloped, tree-covered areas of the Tanana River floodplain are more distinct in images acquired during thaw conditions. The contrast between the vegetated islands and the unvegetated bars of the Tanana River is also greater during thaw conditions. Dielectric changes in both the snow and vegetation are the probable causes of the increased contrast.

Snow surface conditions on the river varied from loose granular snow to firmer wind-blown and melt crusts. Depth hoar was found below the surface snow at all sites and constituted 16 to 100% of the snowpack where the snow was undisturbed. Depth hoar crystals ranged generally from 1- to 12-mm in size, with an occasional columnar crystal as long as 20 mm. Snow density measurements varied from as low as 0.15 g/cm³ in depth hoar to 0.44 g/cm³ in wind-blown crusts. The densities of compacted snow on surfaces traveled by snowmobiles were from 0.33 to 0.46 g/cm³.

River bed and bars : The river bars and exposed river bed show up as mottled dark areas with variable light and dark tones caused by the irregular surface, scattered vegetation and ephemeral channels. Some of the bars and exposed bed have light-toned lines within them on the SAR images that are likely scarps less than 0.3 to 1 m high which border these old channels.

Band comparisons

Visual comparisons of JPL color composite images made from the HH-, VV- and HV-polarized data in each of P-, L- and C-bands, were made to determine the relative ability of the bands to define the features discussed above. This subjective evaluation suggested that the L-band photo products were better overall for distinguishing ice conditions within the river valley (Melloh and Gatto 1990).

Single-band images for cross-and co-polarizations synthesized from uncalibrated data (Fig. 3) illustrate the greater sensitivity of L- and C-bands compared to P-band for discerning the ice jam at Groin #1. The C-band cross-pol images of March 19 show great sensitivity to the gradation in roughness along the jam, while the L-band images of March 13 show the longitudinal pattern most clearly. The SAR data can be rescaled to bring out more detail in the jams.

CONCLUSION

River ice types and conditions distinguished on the Airborne SAR images show good potential for use of the data in studies of river ice processes and engineering applications. Perhaps the most important of these is that the rough-surfaced ice accumulations, or ice jams, are readily discernible in C- and L-band images, and that texture within the jams may be related to variations in roughness of the accumulations.

ACKNOWLEDGMENTS

We thank Miriam Baltuck and Leo DeGreef of NASA, and Tommy Thompson, Howard Zebker, Yunling Lou, Rose Sanchez, Ben Holt, JoBea Way, John Crawford and Fred Burnette of JPL, for their assistance in obtaining image data. We also thank Edward Chacho (CRREL) for his assistance with field data collection and Steven Arcone, Michael Ferrick, Jon Zufelt and Edward Chacho of CRREL for their review and comments on this manuscript.

REFERENCES

- Arcone, S.A., B.E. Brockett, D.E. Lawson and E.F. Chacho (1987) Evaluation of the magnetic induction conductivity method for detecting frazil ice deposits. CRREL Report 87-17, U.S. Army CRREL, Hanover, NH. 03755-1290.
- Bryan, M.L., and R.W. Larson. 1975. The study of fresh-water lake ice using multiplexing imaging radar. Journal of Glaciology, 14(72):445-457.
- Page, D.F. and R.O. Ramseier. 1975. Application of Radar Techniques to Ice and Snow Studies. Journal of Glaciology, 15(73):171,191.
- Melloh, R.A., and L.W. Gatto. 1990. Interpretation of passive and active microwave imagery over snow-covered lakes and rivers near Fairbanks, Alaska. Proceedings of the workshop on Applications of Remote Sensing in Hydrology, National Hydrology Research Centre, Saskatoon, Saskatchewan, 13-14 Feb. 1990.
- Weeks, W.F., A.G. Fountain, M.L. Bryan, and C. Elachi (1978) Differences in radar returns from ice-covered lakes. Journal of Geophysical Research, 83(C8):4069-4073.

**PRELIMINARY RESULTS FROM
THE MAESTRO 1 CAMPAIGN OVER THE BLACK FOREST**

P.N. Churchill, G. De Grandi and A.J. Sieber

**Commission Of The European Communities, Joint Research Centre,
Institute Of Remote Sensing Applications, 21020 Ispra (VA), Italy.**

ABSTRACT

The Joint Research Centre (JRC) Ispra and the European Space Agency (ESA) have co-sponsored the deployment of the National Aeronautics and Space Agency (NASA) and Jet Propulsion Laboratory (JPL) C-, L-, and P-band polarimetric synthetic aperture radar (SAR) in Europe in mid-August 1989. This deployment represents the first opportunity for European agencies and institutes to evaluate the current state of the art of multifrequency polarimetric imaging technology over European Test Sites.

Of particular interest to the Joint Research Centre (JRC) Ispra is the Black Forest Test Site at Freiburg in the Federal Republic of Germany. This Test Site incorporates the Villingen region of the Black Forest to the south-west of Germany. This paper reports upon the activities undertaken in preparation for the MAESTRO 1 Campaign in the Black Forest Test Site. In particular this paper reports upon the ground data collection campaign for the Freiburg Test Site where extensive and intensive ground data measurements were undertaken. These measurements were based upon standard ground data collection protocols developed for forestry by the JRC and utilised throughout Europe for the MAESTRO 1 Campaign. The paper then goes on to present preliminary results derived from the SAR data using the JRC-developed software for polarimetric data interpretation, POLTOOL.

1. INTRODUCTION

In August 1989 the National Aeronautics and Space Agency (NASA) and Jet Propulsion Laboratory (JPL) C-, L-, and P-band polarimetric synthetic aperture radar (SAR) flew a series of overflights over European Test Sites. Of particular interest to the Joint Research Centre (JRC) Ispra is the Black Forest Test Site at Freiburg in the Federal Republic of Germany. This Test Site incorporates the Villingen region of the Black Forest to the south-west of Germany.

The NASA/JPL SAR overflights over the Black Forest were part of a Commission of the European Communities (CEC) JRC Ispra and European Space Agency (ESA) jointly sup-

ported and financed campaign entitled MAESTRO 1. For this Campaign forestry and agricultural applications were chosen as the principal study objectives. On this basis four Test Sites were selected: Landes (France), Freiburg Black Forest (Federal Republic of Germany), Flevoland (The Netherlands) and Thetford (United Kingdom) (JRC/ESA, 1989a). For each Test Site JRC/ESA supported the flight and processing costs for three scenes.

Data from these sites have been made available to scientists and institutes in all CEC and ESA member states via a Call For Experiments (JRC/ESA, 1989b). The results to this Call For Experiments have now been reviewed and as a result there will be 33 studies taking place on the data.

This paper reports upon the activities undertaken in preparation for the MAESTRO 1 Campaign in the Black Forest Test Site. In particular this paper reports upon the ground data collection campaign for the Freiburg Test Site where extensive and intensive ground data measurements were undertaken. These measurements were based upon standard ground data collection protocols developed for forestry by the JRC and utilised throughout Europe for the MAESTRO 1 Campaign. The paper then goes on to present preliminary results derived from the SAR data using the JRC-developed software for polarimetric data interpretation, POLTOOL.

2. THE FREIBURG BLACK FOREST TEST SITE

The Freiburg Black Forest Test Site is of particular interest to the JRC for two reasons. Firstly, the Test Site is that selected for the European component of the ERS-1 pilot project, International Forest Investigation (IFI) (Sieber, 1986). Secondly, the area selected for the MAESTRO 1 Campaign is one that has been under observation, and thus fully mensurated, by the European Centre for Air Pollution Prevention Measures (PEF) since 1984 (PEF, 1990). There is thus an historical data base for the area, with data to be collected for the expected lifetime of ERS-1, plus the opportunity to collect airborne and satellite-borne data over the area for the next years.

The overall objective of the IFI study is to perform coordinated global forest experiments designed to use the unique properties of SAR to characterise the physical nature of forest stands as inputs into ecosystem and climatology models. In particular this, in the European context, involves the following specific objectives:

- to quantify the temporal range of radar returns from a variety of forest canopy types under different growth stages and environmental and seasonal conditions;
- to unfold the components of backscatter from a forest stand using observations made under a variety of environmental conditions;
- to quantify radar signatures in terms of forest ecosystem characteristics;
- to map and monitor human impact on forest canopies, particularly, in the European context, acid deposition.

The Freiburg Black Forest Test Site contains features that are well suited to these objectives. The site itself incorporates boreal forest, which is typical of Central European forest, with the major tree species for this area being homogeneous stands of *Picea abies*, *Abies alba* and *Pinus sylvestris* ranging in age from 80 – 100 years and in height from 30 – 40 metres. The understory of the stands is comprised of young blueberry, spruce and fir.

In addition, under the auspices of the PEF, water and element flux measurements have been and are being undertaken, with input/output measurements being made on small, defined watersheds (Zottl and Feger, 1990). In these experiments fertiliser has been applied under controlled conditions, particularly Kieserite containing magnesium and sulphur (Feger et al, 1990), in order to study the effects on permanent water and element flux as an indication of the potential effects on forest decline of acid deposition. The data from these studies provide the IFI study with both a mensurated forest site, and with a database of measurements undertaken since 1984.

3. GROUND DATA COLLECTION

In support of the Freiburg study a large ground data collection campaign was undertaken. In order to optimise these data obtained the forest ground data were collected and compiled according to standard protocols (Churchill, 1989). This has been undertaken under the auspices of the European Radar Cross Section database (EURACS) which sets down strict rules for data collection and compilation in order to ensure data compatibility and quality (Churchill and Sieber, 1988).

Using these protocols a full range of ground data were collected. These included 'extensive' data for 25 stands within the Test Site, and 'intensive' data for selected stands. For the 25 stands a series of data were collected that described the topography, species and age composition, and basic tree and stand geometry (tree height, diameter at breast height, tree density and understory composition).

For the stands selected for more intensive measurements detailed measurements were also taken of the tree pressure potential gradient, tree moisture content, bole dielectric constant and stand soil moisture profile. These measurements were undertaken simultaneously on the same trees both on a diurnal basis and during the time of the actual SAR overpasses.

In addition ancillary data describing the meteorological conditions were also collected from the nearby meteorological station at Villingen.

4. OVERFLIGHTS

Three flight lines were successfully flown over the Test Site on the 18th August 1989. These were flown so as to ensure coverage of the site of interest in the near, mid and far ranges with a common centre swath incidence angle of 45⁰.

The 18th August was a warm day of approximately 22⁰C, with a light south-easterly wind (1 on the Beaufort scale) and a 4/8th's cloud cover.

5. PRELIMINARY RESULTS

5.1 Software Tools For Multipolarization Data Analysis

The JRC Ispra has developed a suite of software tools in the SUN OS environment for the processing and presentation of radar polarimetry data. These tools are intended to support in-house, research-oriented, analysis of polarimetric data coming from airborne and space-borne sensors, and are also used by the international remote sensing scientific community to analyze data in the frame of joint campaigns. The tools described in the paper are:

- POLTOOL – a tool for basic radar polarimetry data analysis using Stokes matrix compressed data.

- **SMTOOL** – a research-oriented tool for full resolution scattering matrix data analysis, including the basic data analysis and some exploratory techniques, based on the distribution of the characteristic polarization states.
- **CHAMELEON** – a tool for the synthesis and overlaid presentation of multiple data (different frequencies or same frequency different polarizations).

All tools are written in the SunView windowing environment and run on a distributed system of SUN 4s and SUN 386s. In addition CHAMELEON uses the TAAC accelerator for the synthesis computational kernel and the true color image display.

A detailed description of these tools is given in De Grandi et al (1990); only an overview of their major characteristics will be given here.

5.1.1 POLTOOL: POLTOOL is a software tool for the processing and presentation of SAR multipolarization data in the Stokes representation. It has been developed in cooperation with the Jet Propulsion Laboratory, and part of the computational kernel has been taken by MULTIVIEW, a multipolarization software running in the VAX VMS environment. The tool can be conceptually divided into a computational kernel, a presentation model, a set of accessories and the user's interface.

The computational kernel is based on the Stokes matrix representation of the scattering mechanism; in addition the NASA/JPL scheme for a compressed representation of the Stokes matrix is adopted. From the Stokes matrix the following quantities of interest are derived:

- the power and the amplitude of the scattered wave at a given transmit and receive antenna polarization state;
- the polarization signature over an area of interest (scattering cross section as a function of the polarizations of the transmit and receive antennas);
- the coefficient of variation (minimum received power over maximum received power) for an area of interest;
- the HH–VV phase difference distribution;
- amplitude ratios for any combination of polarisations.

The model for data presentation consists of a set of overlapping windows, where objects are drawn. A main canvas is always present on which the full image at HH polarization is shown. On the main canvas areas of interest can be defined in several modes:

- a square box, scalable in fixed steps;
- a rectangle that can be rubber banded to any dimension;
- a polygon.

Each area is mapped into an object, which is visually characterized by a colour. The computational kernel can then be applied to the object, and suitable presentations of the results spawned. In particular amplitude and power are mapped into an image in a rectangular window, with signatures represented as 3D wire frame plots and 2D flat plots. In addition the coefficient of variation can be presented as an image.

The accessories manipulate objects to obtain new quantities or a new representation of the same quantity. They are:

- the Browser;
- the Image Processor;
- the Batch Command Interpreter;
- the Annotation Record Handler;
- the File Exporter;
- the Extended Services Handler.

The user's interface is based on the SunView models, namely graphic objects like buttons, sliders, icons that are acted upon interactively with a pointing device (mouse). Each object is associated with a help menu; the help menu data base is kept in text files, and can be tailored for different classes of users.

5.1.2 SMTTOOL: SMTTOOL is a tool for the analysis of full resolution scattering matrix data. It is somewhat more research oriented than POLTOOL in the sense that the objective is to explore if there is an advantage in using the full information content of the processed data (no four-look averaging), and to try out some techniques for the characterization of the scatterer using the characteristic polarization state theory. The main operations that can be performed on regions of interest are phase analysis, and the optimum polarization states (OPS) analysis.

In the phase analysis histograms of the phase of the scattering matrix elements (HH, HV, VH, VV) and of the phase differences (HH–VV, HV–VH) are computed and plotted. The phase distribution of the single scattering matrix elements is useful as a quality check on the data set; in particular the HV–VH phase difference distribution is used to make a calibration of the two crosspol channels, whilst the HH–VV phase difference distribution conveys information on the scene properties.

To supplement the information contained in the HH–VV histogram an image of the phase difference is also built, associating 16 colours to phase values, and modulating the intensity of each color with the amplitude of the received wave. Phase is defined from -180° to $+180^\circ$; four colour bins are assigned to each quadrant, and colours wrap around at $+180^\circ$ or -180° .

In the OPS analysis the polarization states of the transmitted signal for which the target returns maxima and minima in the co-polarized channels and cross-polarized channel are calculated for each pixel. This is done by applying a unitary transformation of the scattering matrix to a new vector basis where it becomes diagonal. As a result the states for crosspol nulls can be provided, and the corresponding power in the copol channel can be readily calculated from the eigenvalues of the transformed matrix. Copol nulls are then calculated from the diagonal matrix (crosspol nulls basis), setting the power in the copol channel to zero. Similarly the copol maxima and crosspol maxima are calculated in the crosspol basis.

Histograms are then calculated for the distribution of the minima and maxima as a function of the polarization state; the distributions are grouped into four categories:

- crosspol nulls;
- crosspol maxima;

- copol nulls;
- copol maxima.

Since the polarization state is defined by the orientation and the ellipticity angles, and there are two states in each category, four histograms are plotted for each category.

Utilising this technique information can be extracted about the scatterer using two criteria: the clustering of the OPS [12], and the mapping of selected OPS into the spatial domain. This means that it is possible to reconstruct the position of all the pixels that gave rise to a particular polarization state and highlight those pixels in the amplitude image.

5.1.3 CHAMELEON: CHAMELEON owes its name to its ability to change colours; it is in fact a tool that exploits the true colour capability of the TAAC application accelerator to map information into color planes. Using the three fundamental colour channels (red, green and blue) it is possible to associate to each colour a piece of space-dependent information, and obtain a visual rendition of the global effect of the three pieces of information. In other words it is possible to add a dimension to a bidimensional amplitude image.

CHAMELEON works on three files of compressed Stokes matrix data, and implements the synthesis algorithm for the three channels. Therefore it is possible to have a composite amplitude image of three frequency bands data (P– L– and C– band) synthesized at the same antenna configuration, or an image of the same band but synthesized in three different antenna configurations.

5.2 Preliminary Results

To date only a few scenes of both the four-look Stokes matrix and the single-look scattering matrix data of the MAESTRO 1 campaign have been analysed. In this early phase of the analysis the objective is simply to:

- experiment with the possibilities that the software tools provide;
- test the tools themselves;
- assess the quality of the data;
- perform some correction, such as the HH–VV phase calibration or the reconstruction of missing lines;
- assess whether more functions are required in the tools.

This will lay the ground for a more systematic analysis of the campaign data that will be carried out in the near future.

A number of products have been produced by the preliminary processing; these are:

- Amplitude images for different antenna configurations (mainly HH, HV, VH, VV, linearly polarized at 45 degrees orientation, right-hand and left-hand circularly polarized RHC LHC).
- Ratioed amplitude images for different combinations of transmit and receive antenna configurations (mainly HH/VV, HV/VV, HV/HH, RHC/LHC).
- Power copol and crosspol signatures.
- Phase images (color hue modulated by phase, color intensity modulated by amplitude).

- Phase histograms.
- Coefficient of variation images.
- Stokes matrix parameters images.
- Copol and crosspol nulls histograms.
- True color composite images with overlay of three frequencies or three polarizations and the same frequency.

As an example of one of the results which can be obtained by the software tools described in Section 4 above, the results of a signature analysis over the Freiburg Test Site, using the compressed Stokes data are presented below.

For this analysis copol and crosspol power signatures for three areas have been generated, namely an urban area, a grass land, and a forested area, using three data sets (P– L– and C– band). The signatures for the L– band are shown in Figure 1. POLTOOL has been used for the processing (see Section 4). Each signature is plotted in a SunView window as a flat diagram in the orientation – ellipticity plane (the pixel grey level proportional to power) and as a 3D wire frame; moreover the coefficient of variation (min power over max power) and the pedestal factor (min power/max power – min power) are calculated; these quantities are indicators of the properties of the signature function that in turn can be related to the underlying scattering mechanisms (Evans et al, 1988).

The main characteristics of the signatures together with some comments are given in the following; however caution must be taken before attempting any further interpretation of this data, since the image was not calibrated in phase.

5.2.1. L–band signatures

(a) Grassland: The copol signature has one maximum and the crosspol a deep valley with three minima (highly polarized return); also the crosspol has a small coefficient of variation and low pedestal. This signature approximates the one that we would expect from the model of a slightly rough dielectric surface, where the pedestal is zero, and the minima is at ellipticity 0 for any orientation. The characteristics of this signature are as follows:

Copol Pedestal Coeff.:	5.085104e–01	Crpol Pedestal Coeff.:	1.873531e–01
Copol Variation Coeff.:	3.370944e–01	Crpol Variation Coeff.:	1.577905e–01

(b) Forested Area: This signature demonstrates a high coefficient of variation and high pedestal in the crosspol signature (due to heterogeneity of scatterers and multiple scatter). The characteristics of this signature are as follows:

Copol Pedestal Coeff.:	6.208196e–01	Crpol Pedestal Coeff.:	9.681155e–01
Copol Variation Coeff.:	3.830282e–01	Crpol Variation Coeff.:	4.918998e–01

(c) Urban area: For this signature a double peaked surface and a sloping pedestal are observed along the ellipticity axis; it can be modeled as a combination of double bounce scattering from a dihedral corner reflector and an unpolarized component due to multiple scattering. The signature also demonstrates a low coefficient of variation and low pedestal. Although in the copol there is an asymmetry with respect to the ellipticity angle, for negative angles there is a high pedestal. The characteristics of this signature are as follows:

Copol Pedestal Coeff.:	1.197521e–01	Crpol Pedestal Coeff.:	1.741504e–02
Copol Variation Coeff.:	1.069452e–01	Crpol Variation Coeff.:	1.711695e–02

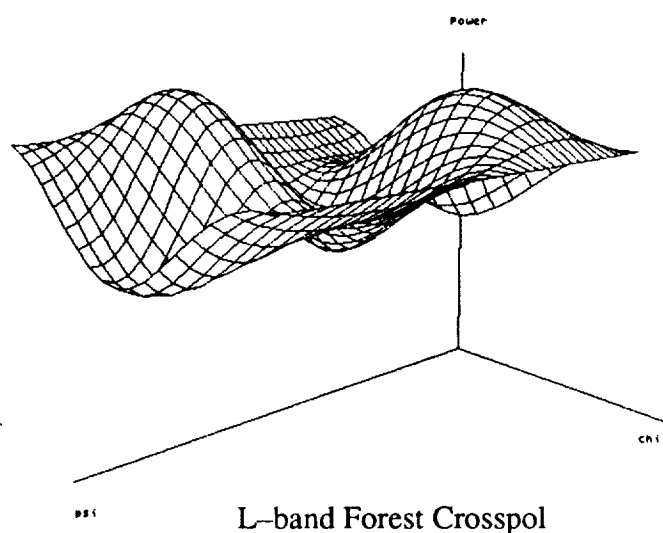
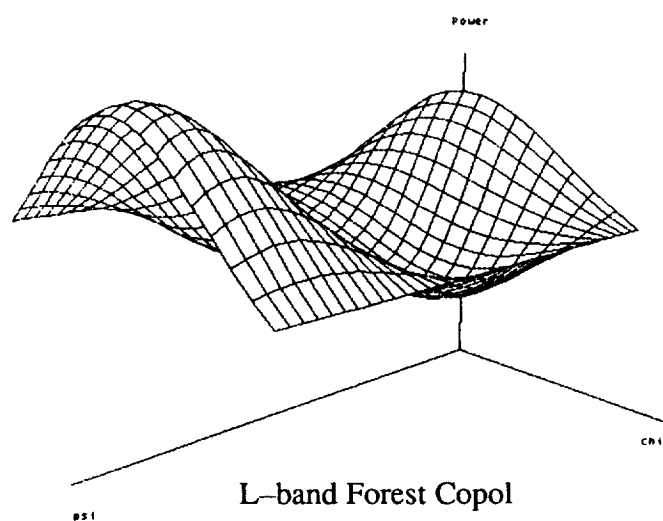
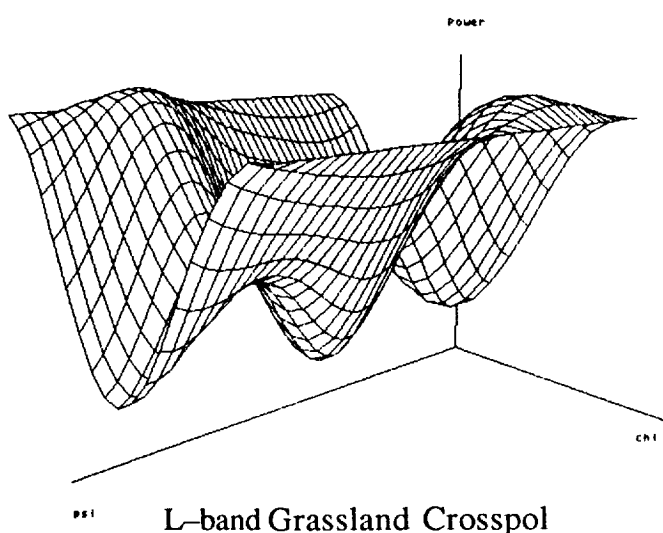
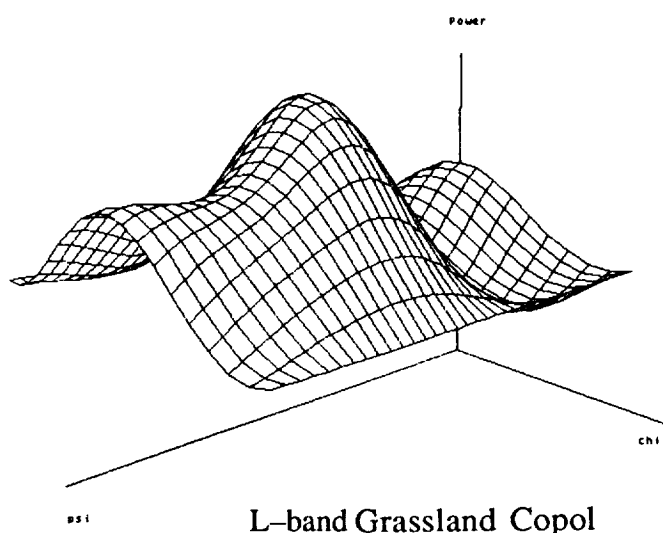
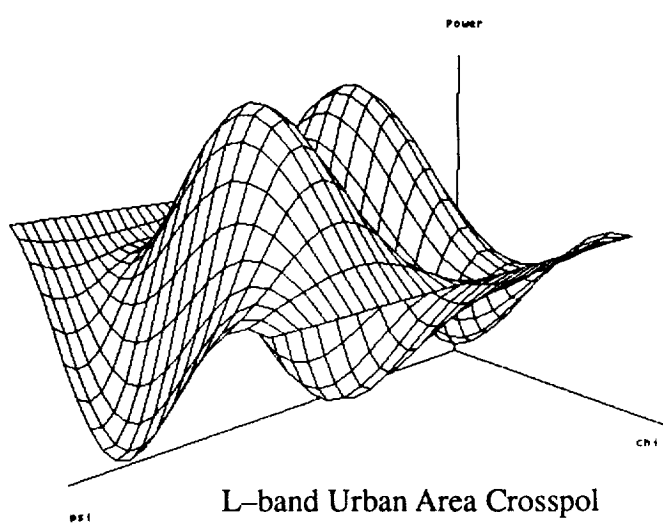
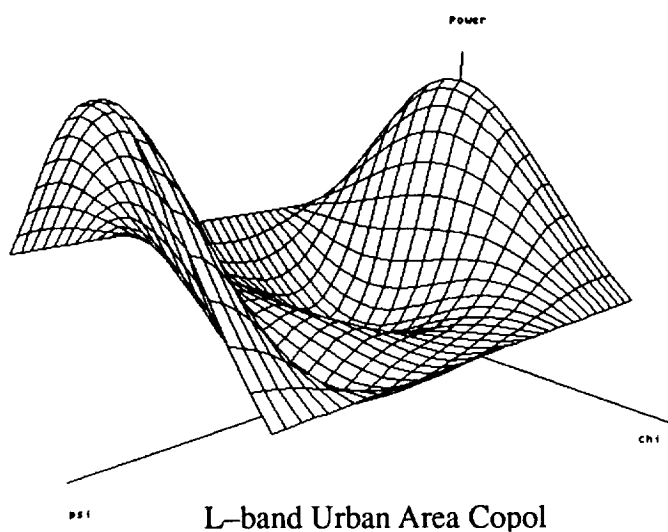


Figure 1. Polarimetric Signatures at L-Band

5.2.2. C-band signatures

(a) Grassland: For grassland the crosspol signature has a double-peaked surface; the two peaks occur at 45^0 and 135^0 (orientation angle). The signature also demonstrates a high pedestal and intermediate coefficient of variation; the copol signature has two dips again at 45^0 and 135^0 (orientation angle).

Therefore this area at C-band no longer behaves as an homogeneous scatter, but assumes characteristics similar to the urban area at L-band. The characteristics of this signature are as follows:

Copol Pedestal Coeff.:	5.375944e-01	Crpol Pedestal Coeff.:	4.692599e-01
Copol Variation Coeff.:	3.496334e-01	Crpol Variation Coeff.:	3.193852e-01

(b) Forested area: These signatures are similar to those of the grassland; the crosspol signature has a double-peaked surface, and the copol surface has two dips. Moreover the crosspol is comparable to the corresponding signature at L-band, although the pedestal is lower. The characteristics of this signature are as follows:

Copol Pedestal Coeff.:	6.166195e-01	Crpol Pedestal Coeff.:	4.702785e-01
Copol Variation Coeff.:	3.814253e-01	Crpol Variation Coeff.:	3.198568e-01

(c) Urban area: For urban areas at L-band the copol signature is similar to that generated at L-band, but with a lower pedestal; the crosspol signature has three deep minima at 0^0 , 90^0 and 180^0 (orientation angle). A low coefficient of variation is also noted in the crosspol signature. The characteristics of this signature are as follows:

Copol Pedestal Coeff.:	1.117043e-01	Crpol Pedestal Coeff.:	3.174420e-02
Copol Variation Coeff.:	1.004802e-01	Crpol Variation Coeff.:	3.076751e-02

5.2.3. P-Band signatures

As a general remark it is noted that the coefficient of variation and the pedestal do not vary much over the three areas.

(a) Grassland: The crosspol signature for grassland at P-band is similar to that for L-band. In addition the copol signature has a much lower relative maximum at 90^0 (orientation angle), and two maxima at 0^0 and 180^0 . The characteristics of this signature are as follows:

Copol Pedestal Coeff.:	3.412435e-01	Crpol Pedestal Coeff.:	1.430704e-01
Copol Variation Coeff.:	2.544232e-01	Crpol Variation Coeff.:	1.251632e-01

(b) Forested area: Both crosspol and copol signatures are similar to those at L-band, but with much lower pedestal and lower coefficient of variation. The characteristics of this signature are as follows:

Copol Pedestal Coeff.:	2.363815e-01	Crpol Pedestal Coeff.:	2.316669e-01
Copol Variation Coeff.:	1.911881e-01	Crpol Variation Coeff.:	1.880922e-01

(c) Urban area: The copol signature is similar to that of the L-band, but with a slightly higher pedestal and coefficient of variation. The crosspol signature is also similar to the L-band, but with higher pedestal and coefficient of variation and different peak-to-valley ratios. The characteristics of this signature are as follows:

Copol Pedestal Coeff.:	2.688297e-01	Crpol Pedestal Coeff.:	2.374326e-01
Copol Variation Coeff.:	2.118722e-01	Crpol Variation Coeff.:	1.918752e-01

6. CONCLUSIONS

This paper has presented some preliminary results concerning the European MAESTRO 1 Campaign, with particular reference to the Freiburg Black Forest Test Site. The paper has reported upon the preparations undertaken for the MAESTRO 1 Campaign in particular in terms of the ground data collection. The paper then has presented some preliminary results derived from the SAR data using the JRC-developed data analysis software. These analyses will now be continued, both at the JRC, and at institutes from all over Europe.

7. REFERENCES

- Churchill, P.N., (1989), "Procedures for the collection and compilation of forest ground data in microwave experiments," JRC Ispra Technical Note, July.
- Churchill, P.N., and Sieber, A.J. (1988), "EURACS: a European radar cross section data base," Proceedings of IGARSS'88 Symposium, Edinburgh, Scotland, 13–16 Sept., ESA SP-284 (IEEE 88CH2497–6).
- De Grandi, G., De Groof, H., and Sieber, A.J. (1990), "An overview of the software tools for radar multipolarisation data analysis and presentation developed in the SUN OS environment by the JRC Ispra Microwave Team," Proceedings of the SUN Expo Europe'90 Technical Conference, Netherlands Congress Centre, The Hague, April 18–20.
- Evans, D.L., Farr, T.G., Van Zyl, J.J., and Zebker, H.A. (1988), "Radar polarimetry: analysis tools and applications," IEEE Transactions on Geoscience and Remote Sensing, Vol.26, No.6, November.
- Feger, K.-H., Zottl, H.W., and Brahmer, G. (1990), "Project ARINUS: effects of Kieserite fertilisation," Proceedings Projekt Europaisches Forschungszentrum fur Massnahmen zur Luftreinhaltung (PEF), (1990), 6. Statuskolloquium des PEF: Program und Kurzfassungen der Vortrage, Kernforsschungszentrum Karlsruhe, 6–8 March.
- Joint Research Centre and European Space Agency (1989a), "MAESTRO 1 Campaign 1989: experiment plan," Prepared by P.N. Churchill and E.P.W. Attema, July.
- Joint Research Centre and European Space Agency (1989b), "MAESTRO 1 Campaign 1989 airborne synthetic aperture radar (SAR) campaign 1989: call for experiments," Prepared by P.N. Churchill and E.P.W. Attema, July.
- Projekt Europaisches Forschungszentrum fur Massnahmen zur Luftreinhaltung (PEF), (1990), "6. Statuskolloquium des PEF: Program und Kurzfassungen der Vortrage," Kernforsschungszentrum Karlsruhe, 6–8 March.
- Sieber, A.J. (1986), "International forest inventory: the global forest ecosystem as viewed by ERS-1," ERS-1 Proposal, JRC Ispra, T.N.I.04.E2.86.105, November.
- Zottl, H.W., and Feger, K.-H. (1990), "Forest ecosystem research at the ARINUS sites Schuchsee and Villingen," Proceedings Projekt Europaisches Forschungszentrum fur Massnahmen zur Luftreinhaltung (PEF), (1990), 6. Statuskolloquium des PEF: Program und Kurzfassungen der Vortrage, Kernforsschungszentrum Karlsruhe, 6–8 March.

APPLICATION OF THE SEMIVARIOGRAM TEXTURAL
CLASSIFIER (STC) TO SIR-B DATA OF BORNEO

F.P. MIRANDA, J.A. MACDONALD, and J.R. CARR
Mackay School of Mines, University of Nevada, Reno
Reno, NV 89557-0047

INTRODUCTION

This paper presents the results of an application of the semivariogram textural classifier (STC; see MacDonald et al., 1990) to SIR-B data. Ford and Casey (1988) performed a visual interpretation of a SIR-B image of a tropical rain forest in Borneo in which they recognized and mapped three units of forest canopy (coastal lowland forest, tidal forest and swamp) and two units of open areas (clearcut and wetland) (Figure 1). In this study the same image is classified using the STC in an attempt to emulate their interpretation.

IMAGE CLASSIFICATION TECHNIQUE

The STC uses a supervised parallelepiped-type classifier with a minimum distance to mean check for overlapping classifications. This is a strictly deterministic classifier and therefore provides the option of combining textural and radiometric information. The classification process consists of two major subprocesses: training and classification.

Four classes are used in this experiment (Figure 2): water [1], tidal forest [2], coastal lowland forest [3] and swamp [4]. The training subprocess begins with the definition of a mask (22 by 22 pixels) for each class, under which the training is performed (Table 1). The STC then calculates a semivariogram within a moving window (7 by 7 pixels) for each pixel in the training mask. This procedure results in a mean and standard deviation value for each lag distance (up to six) in each class. A mean and standard deviation are also calculated for the DN values of each class.

The classification subprocess begins with the definition of a parallelepiped (PPD). The PPD defines boundary conditions for each class based upon a multiple of the standard deviation from the mean (in our case, this value is 2.00). Then, beginning in the upper left corner of the scene, a semivariogram is calculated for the window surrounding each pixel (keeping the same dimension as the moving window used in the training subprocess). The resulting semivariogram, along with the DN value of the central pixel, are compared with the PPD values. If the value for each lag distance and the DN are situated between the minimum and maximum boundaries for any class, then the pixel is defined as belonging to that class. In the event of overlapping classification, a minimum distance to mean calculation is performed for each possibility, with the lowest value determining the assigned class.

RESULTS

The results of the classification show a high correlation with the map published by Ford and Casey (compare Figures 1 and 3). This is especially true with respect to swamp, coastal lowland forest and tidal forest in the upper left portion of the image. We believe the STC improves the discrimination between swamp and coastal lowland forest in some areas (e.g. location A in Figure 3). Regions of open area units (wetlands and clearcuts) are not included in the training process. As a result they tend to be associated with clusters of non-classified pixels (B, C and D). The classification results also suggest that coastal lowland forest and tidal forest occur interspersed with each other in the central portion of the image (E). This result is not portrayed in Ford and Casey's map. Water constitutes the worst classification result of the present study due to noise in the data. Increased local DN variance (as a result of noise) in the bottom portion of the image resulted in the misclassification of water as tidal forest (location F).

CONCLUSIONS

The results of this study indicate that the STC is a valuable tool for mapping rain forest environments using L-band - HH polarization spaceborne radars. In the first half of the 1990s, the Japanese Earth Resources Satellite (JERS-1) will include a radar system with characteristics similar to SIR-B. The analysis of such a global data set using the STC may provide the Global Change Research Program with invaluable information about remote and perennially cloud-covered tropical regions of the world.

Table 1. Statistical moments of water and vegetation training masks

Surface cover type	DN Mean	DN Variance
Water	38.17	12.11
Tidal forest	83.58	85.43
Coastal lowland forest	110.81	131.25
Swamp	161.34	471.43

REFERENCES

- Ford, J.P., and D.J. Casey, 1988, Shuttle radar mapping with diverse incidence angles in the rain forest of Borneo: Int. J. Remote Sensing, v.9, p. 927-943.
- MacDonald, J.A., F.P.Miranda, and J.R. Carr, 1990, Textural image classification using variograms: paper presented at SPIE's 1990 Technical Symposium on Optical Engineering and Photonics in Aerospace Sensing, 16-20 April 1990, Orlando, Florida.

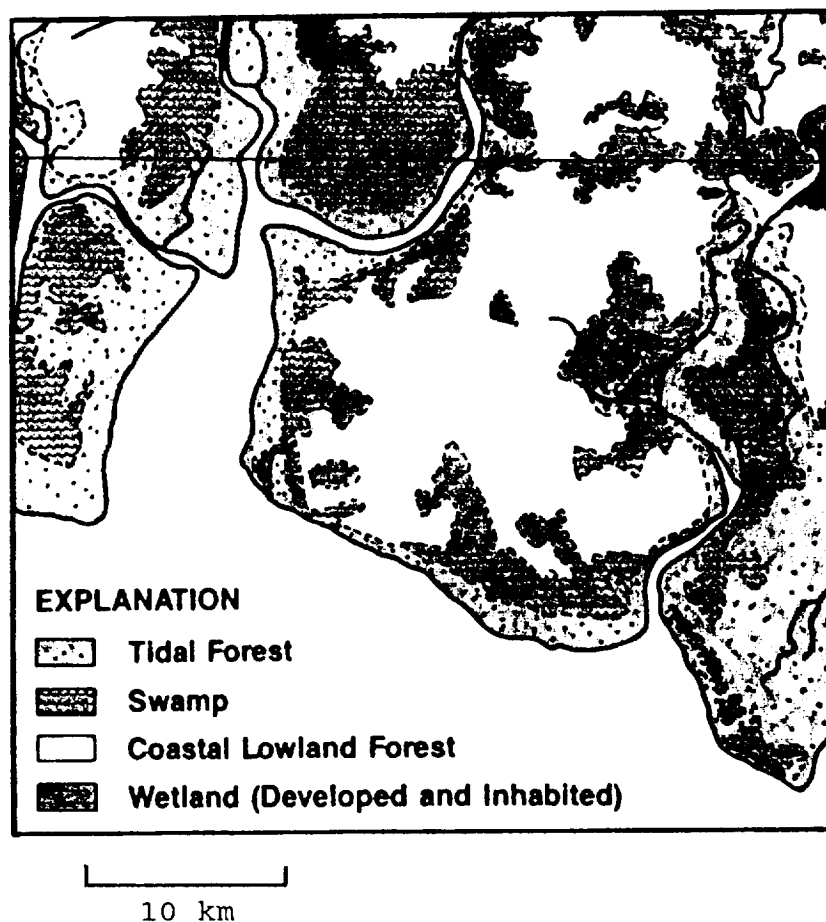


Fig. 1. Surface units mapped from SIR-B image of coastal lowlands, Borneo (After Ford and Casey, 1988)



Fig. 2. Training masks for water (1), tidal forest (2), coastal lowland forest (3), and swamp (4)

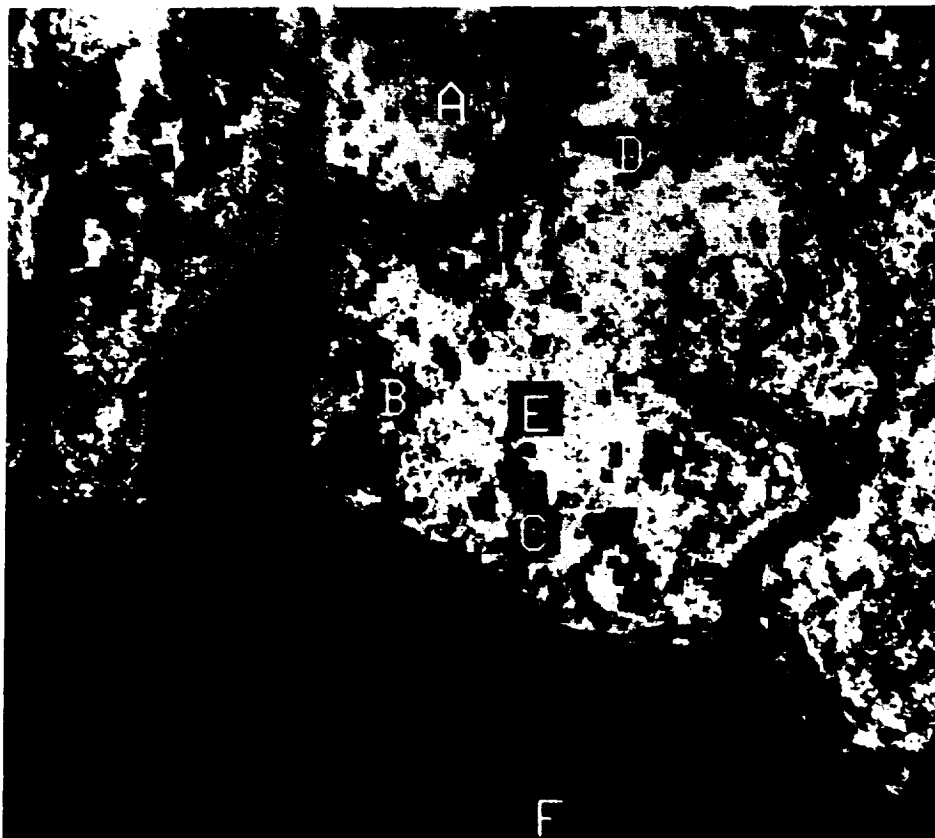


Fig. 3. Classification result. Water = blue, tidal forest = green, coastal lowland forest = yellow, swamp = red

CONFIDENTIAL

Appendix A
Workshop Agenda

AGENDA

AIRBORNE GEOSCIENCE WORKSHOP: AIRSAR

June 7 and 8, 1990

Jet Propulsion Laboratory
von Karman Auditorium

THURSDAY, JUNE 7, 1990

- 8:00 Shuttle Departs Pasadena Holiday Inn for JPL
- 8:30 Welcome and Agenda: M. Kobrick
- 8:40 Program Overview: J. van Zyl
- 8:50 Spring '90 Campaign Review, Summer '90 Campaign Preview: M. Kobrick
- 9:00 AIRSAR Hardware Status/Upgrades/Calibration: K. Wheeler, Y. Shen
- 9:40 Data Products Changes/Issues: R. Carande
- 10:00 BREAK
- 10:30 Calibration of DC-8 SAR Data: Anthony Freeman
- 11:00 Ground Truth Measurements for the Analysis of Airborne SAR Data Recorded Over Oberpfaffenhofen, FRG, 1989: Thomas Bayer, F. Wieneke, R. Winter
- 11:30 Dutch X-Band SLAR Calibration: J. S. Groot
- 12:00 LUNCH
- 1:00 Polarimetric Calibration Using In-scene Reflectors: S. Yuen, J. Kong
- 1:30 Derivation of Surface Roughness from Multifrequency Radar Images: Tom G. Farr, J. van Zyl, F. Burnette
- 2:00 Terrain Statistics for Death Valley and Sand Penetration Experiments: Gerald G. Schaber
- 2:30 Studies of Aeolian Processes with Calibrated AIRSAR Data (Title Only): Lisa Gaddis, R. Greeley, N. Lancaster

- 2:30 Analysis of Multifrequency SAR Observations of the Greenland Ice Sheet:
John Crawford, K. Jezek, R. Bindenschandler
- 3:00 BREAK
- 3:30 Comparison of Active and Passive Microwave Signatures of Arctic Sea Ice:
Mark Drinkwater, J. Crawford
- 4:00 River and Lake Ice Conditions as Determined from AIRSAR Imagery:
Lawrence Gatto, Rae Melloh
- 4:30 Airborne SAR Experiments at the Oetzal Test Site (Title Only):
Dr. Helmut Rott
- 4:30 Mapping ARID Terrains Surface Properties with AIRSAR:
J. Plaut
- 5:00 Shuttle Departs JPL for Pasadena Holiday Inn

FRIDAY, JUNE 8, 1990

- 8:00 Shuttle Departs Pasadena Holiday Inn for JPL
- 8:30 Waves of the Future: Interferometry:
Richard M. Goldstein
- 9:00 Gulfstream Studies with SAR:
Gaspar Valenzuela
- 9:30 Comparison of MIMICS Predictions of Radar Backscatter and Extinction with
Airborne SAR Observations of Boreal Forests in Winter:
Craig Dobson, K. McDonald, E. S. Kasischke, J. B. Way, F. T. Ulaby
- 10:00 BREAK
- 10:15 Effects of Seasonal Change on the Backscatter and Polarization Signatures of
Taiga Forests in Alaska:
JoBea Way, M. C. Dobson, J. Holt, A. Freeman, R. Kwok, E. Rignot
- 10:45 The Relationships Between Total Above-ground Biomass in Loblolly Pine Forest
and Radar Backscatter:
Eric S. Kasischke, N. L. Christensen, M. C. Dobson, D. Beverstock
- 11:15 Preliminary Results from the MAESTRO-1 Campaign over the Black Forest:
Alois Sieber, P. N. Churchill

- 11:45 Theory and Observation of Foliage Penetration Phenomena with Synthetic
Aperture Radar: Howard A. Zebker
- 12:15 Application of the Variogram Textural Classifier to SIR-B Data of Borneo:
F. Miranda, J. MacDonald, J. Carr
- 1:30 Shuttle Departs JPL for Pasadena Holiday Inn

